

Targeted Apoptosis of Senescent Cells Restores Tissue Homeostasis in Response to Chemotoxicity and Aging

Marjolein P. Baar¹, Renata M.C. Brandt¹, Diana A. Putavet¹, Julian D.D. Klein¹, Kasper W.J. Derks¹, Benjamin R. M. Bourgeois⁷, Sarah Stryeck⁷, Yvonne Rijksen¹, Hester van Willigenburg¹, Danny A. Feijtel¹, Ingrid van der Pluijm^{1,4}, Jeroen Essers^{1,4,5}, Wiggert A. van Cappellen², Wilfred F.J. van IJcken³, Adriaan B. Houtsmuller², Joris Pothof¹, Ron W.F. de Bruin⁶, Tobias Madl⁷, Jan H.J. Hoeijmakers¹, Judith Campisi^{8,9}, Peter L.J. de Keizer^{1,8,10,11}

¹ Department of Molecular Genetics, ² Erasmus Optical Imaging Center and Department of Pathology,

³ Department of Cell Biology, ⁴ Department of Vascular Surgery, ⁵ Department of Radiation Oncology,

⁶ Department of Surgery

Erasmus University Medical Center Rotterdam, Wytemaweg 80, 3015CN, Rotterdam, the Netherlands

⁷ Institute of Molecular Biology & Biochemistry, Center of Molecular Medicine, Medical University of Graz, 8010 Graz, Austria

⁸ The Buck Institute for Research on Aging, 8001 Redwood Blvd., Novato, CA 94945, USA

⁹ Lawrence Berkeley National Laboratories, Berkeley, CA, USA

¹⁰ Lead contact

¹¹ To whom correspondence should be addressed: p.dekeizer@erasmusmc.nl

Summary

The accumulation of irreparable cellular damage restricts healthspan after acute stress or natural aging. Senescent cells are thought to impair tissue function and their genetic clearance can delay features of aging. Identifying how senescent cells avoid apoptosis allows for the prospective design of anti-senescence compounds to address whether homeostasis can also be restored.

Here, we identify FOXO4 as a pivot in senescent cell viability. We designed a FOXO4 peptide which perturbs the FOXO4 interaction with p53. In senescent cells, this selectively causes p53 nuclear exclusion and cell-intrinsic apoptosis. Under conditions where it was well tolerated *in vivo*, this FOXO4 peptide neutralized Doxorubicin-induced chemotoxicity. Moreover, it restored fitness, fur density and renal function in both fast aging *Xpd*^{TTD/TTD} and naturally aged mice. Thus, therapeutic targeting of senescent cells is feasible under conditions where loss of health has already occurred and in doing so tissue homeostasis can effectively be restored.

Introduction

Unresolved DNA damage can impair cellular function, promote disease development and accelerate aging (Lopez-Otin et al., 2013). To prevent such undesired consequences, cells are equipped with a range of DNA repair mechanisms (Hoeijmakers, 2009). However, these mechanisms are not flawless. When repair falls short, tissue integrity is still at least initially maintained by independent stress-response mechanisms as apoptosis and cellular senescence (de Keizer, 2017). Senescent cells are permanently withdrawn from the cell cycle and generally develop a persistent pro-inflammatory phenotype, called the Senescence-Associated Secretory Phenotype or SASP (Coppe et al., 2008). The SASP influences the cellular microenvironment, which can be beneficial early in life, or in an acute setting of wound healing (Demaria et al., 2014; Munoz-Espin et al., 2013). However, unlike apoptotic cells, which are permanently eliminated, senescent cells can prevail for prolonged periods of time and accumulate with age (Krishnamurthy et al., 2004). Because of their low, but chronic SASP, persistent senescent cells are thought to accelerate aging and the onset of age-related diseases (de Keizer, 2017). Indeed, senescence has been associated with a plethora of (age-related) pathologies and, conversely, genetic clearance of senescent cells can delay features of aging (Baker et al., 2016). It remains largely unclear how damaged

cells avoid apoptosis in favor of senescence. We set out to address this question and to determine whether therapeutic targeting of senescent cells could not only delay, but also counteract the loss of tissue homeostasis after acute damaging medical treatments as chemotherapy, or chronic damage causer either by accelerated or natural aging.

Results

FOXO4 is elevated in senescent cells and maintains their viability

To identify potential pivots in senescent cell viability, we initiated this study by investigating whether apoptosis-related pathways are altered in senescent cells. We performed unbiased RNA sequencing on samples of genomically stable primary human IMR90 fibroblasts and IMR90 induced to senesce by Ionizing Radiation (Rodier et al., 2011). As senescent cells are reportedly apoptosis-resistant (Wang, 1995), we expected pro-apoptotic genes to be repressed. Surprisingly, however, senescent IMR90 showed an upregulation of prominent pro-apoptotic “initiators” PUMA and BIM while the anti-apoptotic “guardian” BCL-2 was reduced (Fig. 1A + S1A). This suggested senescent IMR90 are primed to undergo apoptosis, but that the execution of the death program is restrained. We reasoned such a brake could potentially be a transcriptional regulator and focused on transcription factors that have previously been linked to apoptosis, including STAT1, 2 and 4, RELB, NFκB, TP53 and FOXO4 (Fig. 1B + S1B). Interference with JAK-STAT signaling is known not to affect the viability of senescent cells (Xu et al., 2015) and we have previously observed similar effects for NFκB and p53 inhibition (Freund et al., 2011; Rodier et al., 2009). Our interest was therefore directed to a factor that has not yet been studied as such, FOXO4 (Fig. 1B). FOXO4 belongs to a larger mammalian family, with FOXO1 and 3 being its major siblings. FOXOs are well studied in aging and tissue homeostasis as targets of Insulin/IGF signaling and as regulators of Reactive Oxygen Species (de Keizer et al., 2011; Eijkelenboom and Burgering, 2013; Martins et al., 2016). Whereas senescence-inducing IR showed only mild effects on the expression of FOXO1 and 3, both FOXO4 mRNA and protein expression progressively increased (Fig. 1C+D). We therefore wondered whether FOXO4 could function to balance senescence and apoptosis. We stably inhibited FOXO4 expression using lentiviral shRNA (Fig. 1E). FOXO4 inhibition prior to senescence-induction resulted in a release of mitochondrial Cytochrome C (Fig. 1F) and BAX/BAK-dependent Caspase-3 cleavage (Fig. 1G). In addition, FOXO4

inhibition in cells that were already senescent, but not their control counterparts, reduced viability and cell density (Fig. 1H +S1C). Together, this shows that after acute damage FOXO4 favors senescence over apoptosis and maintains viability of senescent cells by repressing their apoptosis response.

FOXO4-DRI disrupts PML/DNA-SCARS and releases active p53 in senescent cells

Interference with FOXO4 signaling could be a strategy to eliminate senescent cells and thereby potentially target senescence-related diseases. However, shRNA-mediated repression of FOXO4 would be complicated to translate to the clinic. Thus, we decided to design compounds that could structurally interfere with FOXO4 function instead. Immunofluorescence experiments showed FOXO4 to be gradually recruited to euchromatin foci after senescence-induction (Fig. 2A-C+ S2A-D). As senescence develops, PML bodies fuse with 53BP1-containing DNA-SCARS to jointly regulate expression of the SASP(Rodier et al., 2011). High resolution Structured Illumination Microscopy (SIM) of nuclei of senescent cells showed FOXO4 to reside within these PML bodies, adjacent to 53BP1-containing DNA-SCARS (Fig. 2D; Mov.1+2; Fig. S2E-I).

p53 controls both apoptosis and senescence(Kruiswijk et al., 2015) and localizes to DNA-SCARS in senescent cells(Rodier et al., 2011). Under those conditions p53 is phosphorylated by ATM on Ser15, which blocks its MDM2-mediated degradation(Rodier et al., 2009). Consistent with the observation of FOXO4 residing in PML bodies, FOXO4 localized next to phosphorylated ATM substrates (Fig. S2I) and pS15-phosphorylated p53 (Fig. 2E). This raised the question whether FOXO4 could maintain senescent cell viability by binding p53 and inhibiting p53-mediated apoptosis in favor of cell cycle arrest.

FOXOs can interact with p53, and the interaction domain has been characterized by NMR (Wang et al., 2008). To interfere with the FOXO4-p53 interaction, we therefore designed a cell-permeable peptide comprising part of the p53-interaction domain in FOXO4 (Fig. 2F+G). FOXO1 and FOXO3 are essential to numerous endogenous processes as development, differentiation and tumor suppression, roles not prominently attributed to FOXO4(Hosaka et al., 2004; Nakae et al., 2003; Paik et al., 2007; Renault et al., 2009). Another difference with FOXO1 and 3 is that FOXO4 is only marginally expressed in most tissues (Fig. S2J+K) and FOXO4 knockout mice do not show a striking phenotype (Hosaka et al., 2004; Paik et al.,

2007). We therefore chose a region in FOXO4 that is conserved in both humans and mice, but differs from FOXO1 and FOXO3 (Fig. S2L).

Research on peptide chemistry has shown that protein domains containing natural L-peptides can sometimes be mimicked by using D-amino acids in a retro-reversed sequence (Guichard et al., 1994). Modification of peptides to such a D-Retro Inverso (DRI)-isoform can render peptides new chemical properties, which may improve their potency *in vitro* and *in vivo* (Borsello et al., 2003). Several DRI-modified peptides have been shown to be well tolerated and therapeutically effective in clinical trials. These include a double blinded, randomized, placebo-controlled Phase IIb trial (Beydoun et al., 2015; Deloche et al., 2014; Suckfuell et al., 2014) and a Phase I trial for systemic treatment of solid tumors (Warso et al., 2013), together showing there is precedence for DRI peptides in clinical therapy. This provided the rationale for designing the FOXO4 peptide in a DRI conformation, henceforth named FOXO4-DRI. We performed competition experiments by NMR to investigate whether FOXO4-DRI can inhibit the interaction between p53 and FOXO4 *in vitro*. Titration of a recombinant N-terminal domain of p53 (aa1-312) to a solution containing the ¹H, ¹⁵N-labelled FOXO4 Forkhead (FH) Domain (aa486-206) induced a progressive chemical shift perturbation (CSPs) of ¹H, ¹⁵N HSQC cross peaks, indicating specific binding of p53 to FOXO4 (Fig. 2H). Stepwise addition of the FOXO4-DRI peptide to this complex caused the CSPs of FOXO4 to be reverted back to the unbound state, indicating FOXO4-DRI competes with FOXO4 for p53 binding in a dose-dependent manner and doing so with higher affinity (Fig. 2I).

To facilitate cellular uptake of FOXO4-DRI, it was designed as a fusion with HIV-TAT, a basic and hydrophilic sequence which allows energy-independent cellular uptake of cargo through transient pore formation (Herce and Garcia, 2007). Using an antibody against HIV-TAT, we observed FOXO4-DRI to be taken up as soon as 2-4h after administration and to remain detectable for at least 72h (Fig. 2J). Given that the affinity of antibodies is generally low, this indicates FOXO4-DRI effectively enters senescent cells at high intracellular concentrations, which remain abundant and stable over a prolonged period of time. Following its uptake, FOXO4-DRI reduced the number of senescence-induced FOXO4 foci, PML bodies and 53BP1 DNA-SCARS, while not affecting the number of small 53BP1 foci (Fig. 2K).

FOXO4 can regulate expression of the p53-target p21^{cip1} in senescent cells (de Keizer et al., 2010) and through p21^{cip1}, p53 can induce p16^{in4a}-independent cell cycle arrest in senescent cells (Di et al., 1994).

Moreover, p53 can induce apoptosis either through transactivating pro-apoptosis genes, but also in a transcription-independent manner by translocating to the mitochondria (Mihara et al., 2003). Examination of the promoter of Cdkn1a, the gene encoding p21^{Cip1}, showed a canonical FOXO target sequence to be flanked by two p53 binding sites (Fig. 2L). We therefore investigated the effect of FOXO4-DRI on p21^{Cip1} and p53. FOXO4-DRI reduced senescence-associated p21^{Cip1} levels (Fig. L) and promoted the accumulation and nuclear exclusion of active pSer15-p53 (Fig. 2M + S2M). Together, these results show that by competing with endogenous FOXO4 for p53 binding, FOXO4-DRI disrupts senescence-associated FOXO4/PML/DNA-SCARS and causes nuclear exclusion of active p53.

FOXO4-DRI can selectively and potently target senescent cells for p53-dependent apoptosis

Given the reported pro-apoptotic role of active p53 when recruited to mitochondria, we next assessed the effects on senescent cell viability. Incubation of senescent and control IMR90 with increasing concentrations of FOXO4-DRI showed FOXO4-DRI to potently and selectively (11.73 fold difference) reduce the viability of senescent vs. control IMR90 (Fig. 3A) and other normal cells (Fig. S3A). Real-time cell density measurements revealed the effect to occur as soon as 24-36 hours after administration (Fig. 3B). Neither the same peptide in L-isoform (Fig. 3C), nor an unrelated DRI-peptide based on a distinct Forkhead protein, FOXM1 (Kruiswijk et al., 2016), affected senescent cell viability (Fig. 3D). These results show that FOXO4-DRI can target senescent cells and highlight the importance of the DRI-modification for its potency.

Two classes of anti-senescence compounds have been reported so far: Quercetin/Dasatinib, either alone or in combination (Zhu et al., 2015), and the pan-BCL inhibitors ABT-263/737 (Chang et al., 2016; Yosef et al., 2016). Quercetin and Dasatinib have been reported to be non-specific (Chang et al., 2016). We found no selectivity towards senescent IMR90 (Fig. S3B), and therefore this cocktail was not explored further. ABT-263 (Chang et al., 2016) and ABT-737 (Yosef et al., 2016) target the BCL-2/W/XL family of anti-apoptotic guardians (See also Fig. 1A). Indeed, ABT-737 showed selectivity for senescent IMR90 (Fig. S3B). However, already at low doses it appeared to influence control cells as well (Fig. S3B). Also in a treatment regimen where both compounds were added in consecutive rounds of lower concentrations FOXO4-DRI proved to be selective against senescence yet safe to normal cells (Fig. 3E + S3C).

We next addressed the role of p53 in FOXO4-DRI-mediated clearance of senescent cells. Stable knock-down of p53 reduced the ability of FOXO4-DRI to target senescent IMR90 (Fig. 3F + S3D). A similar effect was observed when the senescent cells were co-incubated with the pan-caspase inhibitors QVD-OPH or ZVAD-FMK (Fig. 3G), suggesting a Caspase-dependent effect. Indeed, real-time imaging in the presence of a Caspase-3/7-activatable dye showed FOXO4-DRI to specifically induce Caspase-3/7 activation in senescent, but not control, cells (Fig. 3H + Mov. 3+4). Together, these data show that FOXO4-DRI potently and selectively reduces the viability of senescent cells by competing with FOXO4-p53 binding, thereby triggering release of active p53 to the cytosol and inducing cell-intrinsic apoptosis through Caspase-3/7. This establishes FOXO4-DRI as a genuine inducer of TASC: Targeted Apoptosis of Senescent Cells.

FOXO4-DRI counteracts chemotherapy-induced senescence and loss of liver function

Given the potency of FOXO4-DRI against senescence *in vitro*, we wondered whether FOXO4-DRI could be of therapeutic use against senescence-related pathologies. We therefore employed three independent *in vivo* senescence-models, one for chemotoxicity (Fig. 4), one for accelerated aging (Fig. 5+6) and one for natural aging (Fig. 7). In all of these, we made use of the recently developed senescence-detection system: p16::3MR. In this system, the promoter of the major senescence gene p16^{ink4a} drives expression of Renilla Luciferase (RLUC) to allow longitudinal visualization of senescence. In addition, it expresses a Thymidine Kinase from the Herpes Simplex virus, which induces apoptosis when cells are presented with its substrate Ganciclovir (Fig. S4A and (Demaria et al., 2014)).

Off-target toxicity limits the maximum tolerated dose of chemotherapeutic drugs and causes long term health problems in cancer survivors, including an acceleration of aging (Henderson et al., 2014). Chemotherapy can induce senescence (Ewald et al., 2010), and we therefore determined whether therapeutic removal of senescence could influence chemotoxicity. As an example, we used the common chemotherapeutic drug Doxorubicin, which can indeed induce senescence (Cahu et al., 2012; Roninson, 2003) and liver toxicity in rodents and humans (Damodar et al., 2014). In agreement with these reports, Doxorubicin induced senescence in IMR90 *in vitro*, evident by elevated SA- β -GAL activity, expression of p16^{ink4a}, and the early and late SASP factors IL-1 α and IL-6 (Orjalo et al., 2009), respectively (Fig. 4A-C; S4B). As seen for IR-senescent cells (Fig. 2+3), Doxorubicin-induced senescent cells showed an

upregulation in FOXO4 foci (Fig.4B+C) and FOXO4-DRI potently and selectively lowered the viability of Doxorubicin-senescent vs. control IMR90 (Fig. 4D). In line with the IR-senescence data, low effective doses of FOXO4-DRI were well tolerated in normal IMR90 compared to ABT-737, while being very potent against Doxorubicin-senescent cells at higher doses (Fig. 4E). Also in this setting, the potency of FOXO4-DRI was more pronounced when applied in consecutive rounds (Fig. 4F + S4C).

It could be that FOXO4-DRI merely lowers the threshold for cells to enter apoptosis after DNA damage. This would impair its potential for *in vivo* or clinical translation. Incubation of normal IMR90 with FOXO4-DRI, administered at various time-points prior to Doxorubicin-exposure, did not influence the sensitivity of cells to Doxorubicin (Fig. 4G). In contrast, Doxorubicin-senescent cells were effectively cleared. Thus, FOXO4-DRI does not predispose healthy cells to DNA-damage, but selectively targets cells that have undergone senescence as a consequence of earlier Doxorubicin-exposure. Together this prompted us to try a similar sequential treatment regimen of FOXO4-DRI in Doxorubicin-exposed mice *in vivo*.

In follow-up of the *in vitro* data, Doxorubicin progressively induced senescence *in vivo* as detected by p16^{ink4a}-driven RLuc in p16::3MR mice (Fig. S4D). Furthermore, as seen in patients, Doxorubicin reduced total body weight (Fig. 4J) and induced expression of FOXO4 foci and IL-6 in the liver (Fig. 4K+L). Strikingly, these effects were neutralized after sequential treatment with FOXO4-DRI (Fig. H-L). We therefore wondered whether liver function was also affected. Doxorubicin strongly induce plasma levels of Aspartate Aminotransferase, AST, an established indicator of liver damage(Damodar et al., 2014)(Fig. 4M). Excitingly, FOXO4-DRI potently counteracted the Doxorubicin-induced increase in plasma AST (Fig. 4N). To address whether these effects are mediated through clearance of senescence, we combined treatment of FOXO4-DRI with GCV, to facilitate senescence clearance through the TK suicide gene of p16::3MR construct. GCV reduced Doxorubicin-induced p16-RLUC expression (Fig. S4E) and plasma AST levels (Fig. 4M + S4F), indicating AST reduction is indeed caused by clearance of senescent cells. In both cases, FOXO4-DRI did not further enhance these effects. Together, these data indicate that FOXO4-DRI is effective in reducing Doxorubicin-induced senescence *in vitro* and *in vivo* and in doing so neutralizes the Doxorubicin-induced loss in body weight and liver toxicity. Thus, FOXO4-DRI is effective against chemotoxicity.

FOXO4-DRI counteracts senescence and features of frailty in fast aging $Xpd^{TTD/TTD}$ mice

We next wondered whether FOXO4-DRI could influence the healthspan of mice in which senescence and the concomitant loss of tissue homeostasis were not actively induced, but were allowed to develop spontaneously as a consequence of aging. As is the case for humans (Ferrucci et al., 2005), we expected strong biological variation in senescence and the SASP in naturally aged wildtype mice. To reduce the effects of biological noise, we therefore decided to first employ fast aging mice. We sought a model that recapitulates features of natural aging and does not suffer from age-related pathologies caused by other processes as apoptosis (de Keizer, 2017). This we found in $Xpd^{TTD/TTD}$, a model based on the human premature aging syndrome Trichothiodystrophy (TTD) (de Boer et al., 2002; de Boer et al., 1998). Using the p16::3MR reporter system, we observed that already at young age $Xpd^{TTD/TTD}$ animals show high levels of p16-positive senescence (Fig. 5A). As also seen for Doxorubicin-induced senescence, FOXO4-DRI reduced this effect (Fig. 5B), arguing that $Xpd^{TTD/TTD}$ is a valid fast aging model for studying the effects of FOXO4-DRI on spontaneously developed senescence *in vivo*.

Underscoring their aging phenotype, $Xpd^{TTD/TTD}$ mice show accelerated loss of hair (Fig. 5D and (de Boer et al., 1998)). While not initially focused on this phenotype, we observed a robust improvement of fur density in FOXO4-DRI treated $Xpd^{TTD/TTD}$ mice (Fig. 5C+D and S5A). To address this more quantitatively, we determined the infrared-measured abdominal surface temperature of the mice. Due to the lack of fur, the abdominal temperature of $Xpd^{TTD/TTD}$ mice was several degrees higher than wildtype counterparts, an effect reduced by FOXO4-DRI (Fig. 5E). A second unexpected observation was found in the behavior of the treated mice. Whereas $Xpd^{TTD/TTD}$ mice generally show less exploratory behavior compared to wildtype littermates, FOXO4-DRI treated animals were noticeably more active (Fig. S5B). To also investigate this more quantitatively, we scored the responsiveness of the mice to gentle physical stimuli. Despite individual variation, $Xpd^{TTD/TTD}$ mice were on average considerably more responsive to such stimuli after FOXO4-DRI treatment (Fig. 5F). Finally, as a more objective measure of activity, we tracked voluntary physical activity in a set-up in which the mice were continuously housed in cages with free access to running wheels. Despite significant individual differences, $Xpd^{TTD/TTD}$ mice were found to run 1.37 ± 0.54 km/day on average, compared to 9.37 ± 1.1 km/day seen for wildtype mice, arguing they are indeed less

mobile (Fig. 5G). In line with the behavioral results, exposure of the mice to FOXO4-DRI increased running wheel activity over time in the majority of these (Fig.H+I). Together, these results indicate that FOXO4-DRI can reduce cellular senescence and counteract hair loss and general frailty in fast aging $Xpd^{TTD/TTD}$ mice.

FOXO4-DRI counteracts loss of renal function in fast aging $Xpd^{TTD/TTD}$ mice

The phenotypical and behavioral results described above are difficult to connect to a molecular mechanism. We therefore decided to focus on the role of senescence in aging-induced decline in function of specific tissues. Pilot measurements of various metabolites in plasma samples of $Xpd^{TTD/TTD}$ mice suggested they suffer from decreased renal function. As injected compounds tend to accumulate in the kidney, this together argued for investigating the potential of therapeutic removal of senescence in this organ. Urea is secreted through urine, but becomes detectable in the blood when glomerular filtration rates drop. Plasma Urea is therefore a marker of declined renal filtering capacity (Gowda et al., 2010; Lyman, 1986). In fact, it was recently established that semigenetic clearance of senescence can delay the aging-induced increase in plasma Urea, establishing senescence as a culprit for loss of renal filtering capacity during aging (Baker et al., 2016). As evident from the increase in plasma Urea levels, renal function indeed declines in wildtype mice as they age (Fig.6A; 26w vs. 130w). This was faithfully recapitulated early in life in $Xpd^{TTD/TTD}$ (Fig. 6A; 26w WT vs 26w TTD). Both naturally aged wildtype and young $Xpd^{TTD/TTD}$ kidneys showed a strong increase SA- β -GAL activity and IL-6 expression in the tubular regions (Fig. 6B+C). In addition, they also showed a significant increase in tubular cells positive for FOXO4 foci (Fig. 6D), together indicating that both modes show elevated senescence. Using an *ex vivo* system of aged kidney slices FOXO4-DRI induced strong TUNEL positivity within 3 days (Fig. 6E and S6A-D), indicating that FOXO4-DRI can also induce apoptosis in these cells. Altogether this provided rationale for investigating the potency of FOXO4-DRI on tubular senescence and renal function in *in vivo*.

A limitation to the therapeutic potential of the senolytic pan-BCL inhibitors ABT-263/ABT-737 is their tendency to cause severe thrombocytopenia (Schoenwaelder et al., 2011). This is undesirable when actually aiming to restore healthspan of aged individuals. Comparing platelet levels before and 30d after treatment showed FOXO4-DRI not to noticeably influence platelet levels (Fig. 6F) or other whole blood values (Fig. S6E). Neither did it cause deleterious effects on non-proliferative tissues as far as tested, e.g.

the heart (Fig. S6F). Encouraged by the passing of at least these initial safety concerns, we progressed to measuring the effects of FOXO4-DRI on renal senescence and functional capacity. In line with the SA- β -GAL data, tubuli of *Xpd^{TTD/TTD}* kidneys show severe loss of LMNB1 (Fig. 6G), a robust molecular marker of senescence (Freund et al., 2012). This is paralleled with elevated IL-6 (e.g. Fig. 6J), indicative of SASP, and elevated Urea levels in the blood (e.g. Fig. 6K). SASP factors as IL-6 may be the cause for the observed loss in renal function and we wondered how FOXO4-DRI would function under such high-SASP conditions. *In vitro* experiments showed FOXO4-DRI to be more potent against senescent cells in which SASP was transiently boosted by recombinant IL1 α / β or LPS, whereas an IL1 receptor antagonist or the general anti-inflammatory drug Cortisol reduced its potency (Fig. 6H+I). Thus, FOXO4-DRI actually is most effective against senescent cells expressing high levels of SASP and could as such be particularly effective against loss of renal function. Excitingly, while not substantially influencing total body nor kidney weight (Fig. S6G), FOXO4-DRI treatment normalized the percentage of tubular cells lacking LMNB1 (Fig. 6G), the tubular IL-6 elevation (Fig. 6J) and the elevations in plasma Urea levels (Fig. 6K). To address whether this is mediated by senescence-clearance, we again made use of the ability of the 3MR construct to eliminate senescent cells through GCV. As GCV is typically administered i.p., we treated a cohort of *Xpd^{TTD/TTD}-p16::3MR* mice i.p. with FOXO4-DRI and GCV. GVC and FOXO4-DRI induced a comparable reduction in plasma [Urea] in both groups (Fig. 6L). Thus, FOXO4-DRI targets high SASP-expressing senescent cells that have naturally developed in the kidneys of fast aging *Xpd^{TTD/TTD}* mice and in doing so restores kidney homeostasis.

FOXO4-DRI counteracts frailty and loss of renal function in naturally aged mice

Encouraged by these results, we decided to challenge whether FOXO4-DRI could also target senescence and tissue homeostasis in normal mice that were allowed to age naturally. As expected, the biological variation in p16-driven senescence was substantial in aged p16::3MR, compared to young *Xpd^{TTD/TTD}-p16::3MR* (Fig. 7A, and C). The variation in running wheel activity was too large to perform meaningful experiments (Fig. S7A). Nonetheless, while again not influencing platelet levels (Fig. 7B), FOXO4-DRI significantly reduced p16-driven RLUC (Fig 7C), and could improve fur density (Fig. 7D) and responsiveness (Fig. 7E). Furthermore, in the kidneys of these mice FOXO4-DRI increased the number of LMNB1 positive cells (Fig. 7F), reduced IL-6 expression (Fig. 7G) and restored renal filtering capacity

measured by decreased plasma Urea (Fig. 7H). As an extra control, also the plasma levels of a second metabolite indicative of reduced renal function, Creatinine, was measured. Also this was reduced by FOXO4-DRI, independently confirming the beneficial effect of FOXO4-DRI on the restoration of renal filtering capacity in naturally aged mice (Fig. 7I). As seen for the *Xpd^{TTD/TTD}-p16::3MR* mice, i.p administration of FOXO4-DRI or GCV equally reduced plasma Urea and Creatinine levels (Fig. 7J). Thus, senescent cells are causal for the reduction in renal function in fast aging *Xpd^{TTD/TTD}* and naturally aged wildtype mice and by selective targeting of high-SASP expressing senescent cells in the tubuli, FOXO4-DRI can restore kidney homeostasis. By inducing TASC, FOXO4-DRI may thus be a potent drug to restore loss of health after natural aging and is an attractive option to explore further in the battle against those age-related diseases that are at least in part driven by senescence.

Discussion

With life expectancy projected to increase in the foreseeable future (Vaupel, 2010) it is important to develop strategies to extend and restore healthspan. Cell-penetrating peptides are relatively understudied in aging research. Further analysis of their use is warranted, as they serve several major advantages. Counter to broad-range inhibitors, CPPs can in theory target any surface-exposed stretch of amino acids to block specific protein-protein interactions and, in doing so, they can selectively modulate very specific downstream signaling events (Discussed in (de Keizer, 2017)). Other compounds, classified as senolytics, have been described to influence senescent cell viability. As a CPP, FOXO4-DRI differs from these by being designed around a specific amino acid sequence in a molecular target only mildly expressed in most normal tissues (see e.g. Fig. S2J+K). Though a more thorough analysis is required, as least as far as tested here FOXO4-DRI appears to be well tolerated, which is an absolutely critical milestone to pass when aiming to treat relatively healthy aged individuals(de Keizer, 2017).

FOXO4-DRI effectively disrupts the p53-FOXO4 interaction (Fig. 2H+I), but the importance of the FOXO4 protein itself is more complicated in DNA damage and senescence. As FOXO4-DRI causes nuclear exclusion of active p53, the levels of p21^{Cip1} decline (Fig. 2L-N). However, the loss of p21^{Cip1} alone is insufficient to induce apoptosis and was actually shown to induce a senescence-escape instead (Brown et al., 1997). Rather, the exclusion of p53 itself has been reported to induce apoptosis directly when located

to mitochondria (Mihara et al., 2003), thereby explaining the FOXO4-DRI effects. FOXO4 shRNAs induce apoptosis in senescent IMR90 (Fig. 1E-H), arguing that full FOXO4 inhibition might also be of use against senescence. True as this may be, chronic FOXO4 reduction is not advisable as FOXOs play a role in DNA-damage repair and *Foxo4*^{-/-} mice are susceptible to acute damage (Zhou et al., 2009). In contrast to loss of FOXO4, FOXO4-DRI does not sensitize healthy cells to acute DNA damage (Fig. 4G). Thus, while permanent FOXO4 inhibition is inapplicable, the fact that as a CPP it can block a specific protein-protein interaction make FOXO4-DRI selective, and thereby well-tolerated and effective.

Based on these positive effects, it is now possible to envision a point on the horizon where the disease indications are identified that could benefit most from FOXO4-DRI therapy. High SASP-secreting cells are likely to play a much larger role in disease development than more sterile senescent cells. Through SASP, senescent cells may permanently confer a state of stemness in neighboring cells and thereby impair tissue function and renewal, an effect which we recently described in the senescence-stem lock model for aging (de Keizer, 2017). FOXO4-DRI has a strong preference for targeting high-SASP subpopulations of senescent cells, but it is unclear what causes heterogeneity in the SASP. It will be a major achievement to unravel those mechanisms and to steer these such that therapeutic targeting is most beneficial. In that sense, identification of senescence-driven pathologies that rely on SASP may help in optimizing candidates for therapy. *Xpd*^{TTD/TTD} is pleiotropic model for aging that can be effectively used as a basis for such research. It is a well-established model for osteoarthritis, especially in cohorts of older age than we used here (52w) (Botter et al., 2011) and for the unhealthy loss in muscle (sarcopenia) and fat mass (Wijnhoven et al., 2005).

Last, it is relevant to note that independent of aging and age-related diseases, FOXO4-DRI may be of use against the progression, stemness and migration of malignant cancer. Given that SASP factors influence these (Campisi, 2013), it will be particularly interesting to determine whether FOXO4-DRI affects those p53-wt cancer cells that have adopted a more migratory and stem-like state due to reprogramming by chronic SASP exposure. In any case, the here reported beneficial effects of FOXO4-DRI provide a wide range of possibilities for studying the potential of therapeutic removal of senescence against diseases for which few options are available.

Author contributions

Conceptualization: PDK. Methodology: MPB, PDK. Software: KWJD, WVIJ, JP. Validation: MPB, DAP, JDDK, YR, HVW, DAF, PDK. Formal Analysis: MPB, DAP, JDDK, KWJD, BJRMB, SS, HVW, DAF, IVDP, WAVC, TM, PDK. Investigation: MPB, RMBC, DAP, JDDK, KWJD, BJRMB, SS, YR, HVW, DAF, IVDP, TM, PDK. Resources: WVIJ, ABH, JP, RWFDB, TM. Data Curation: KWJD, TM, PDK. Writing – Original Draft: PDK. Writing – Review & Editing: MB, PDK. Visualization: PDK. Supervision: JE, TM, JC, PDK. Project Administration: TM, JH, JC, PDK. Funding Acquisition: ABH, TM, JH, JC, PDK.

Acknowledgements

We thank Felicity Chandler for assistance with IHC experiments, Anne Drabbe and David Brouwer for assistance with *in vivo* experiments, Yanto Ridwan for assistance with CT and IVIS imaging, Yvette van Loon for genotyping of the mice, Martin Viertler for initial NMR experiments, Boudewijn Burgering for fruitful discussions and Petra de Keizer-Burger for critical reading of the manuscript. Judith Campisi is co-founder and shareholder of Unity Pharmaceuticals. Jan Hoeijmakers is co-founder of AgenD. Neither companies have been involved in this research, however.

This work was supported by grants from the NIH: R37-AG009909 (JC), the NIA: PPG AG-17242-02 (JC/JH), the Austrian Science Fund: FWF P28854 (TM) and DK-MCD W1226 (TM), the Royal Netherlands Academy of Arts and Sciences (JH), the Erasmus University Medical Center: EMC fellowship 2013 (PDK), the Dutch Kidney Foundation: Grant 15OP11 (RDB&PDK), and the Dutch Cancer Society: fellowship Buit-4649 (PDK) and project grant EMCR 2014-7141 (PDK).

Figure Legends

Fig. 1: FOXO4 is elevated in senescent normal fibroblasts and ensures their viability

A) Schematic representation of the mRNA expression changes (Fig. S1A) of the cell-intrinsic apoptosis pathway (Tait and Green, 2010) between senescent and control (proliferating) IMR90 fibroblasts. Inset: Immunofluorescence for PUMA, BIM and BCL2. B) Volcano plot comparing transcriptional regulators in senescent vs. control IMR90. (See Fig. S1B for expression and p-values). Dark blue: associated with

apoptosis. Inset, left: RNA expression of the FOXO cluster. N.D. Not detectable. Right: Protein levels of the FOXO cluster. FOXO1 was ectopically expressed as positive control. C) QPCR for changes in FOXO1, 3 and 4 mRNA after senescence-induction by 10Gy IR. $p21^{Cip1}$ (biphasic increase), p53 and ETS2 (biphasic decrease) are included as controls. D) Immunoblot for changes in FOXO3 and 4 protein levels after senescence-induction by 10Gy IR. E) The senescence-induced FOXO4 mRNA expression is successfully countered by two shRNAs. F) Cytochrome-C release assay (left) as measure for apoptosis in the conditions of E), quantified in a histogram (right). G) Induction of cleaved Caspase-3 after senescence induction in (mouse-specific) FOXO4-deprived wildtype or *bax/bak*^{-/-} BMK cells. H) AqueousOne viability (left) and colony density (right; see also Fig. S1C) of control and senescent IMR90 cells transduced with the short hairpins used in E).

Fig. 2: FOXO4 localizes to senescence-associated PML/DNA-SCARS, which contain active p53 and can be disrupted by FOXO4-DRI

A) FOXO4 foci and Senescence-Associated Heterochromatin Structures in senescent IMR90 (See also Fig. S2A-I). Bottom: Intensity plot (arbitrary units) of individual pixels measured by the indicated line. B) Quantification of cells containing ≥ 3 FOXO4 foci in time after senescence-inducing IR. C) FOXO4 foci in senescent cells transduced with the shRNAs against FOXO4 described in 1E). D) Structured Illumination Microscopic (SIM) image of the nucleus of a senescent IMR90 cell stained for FOXO4, 53BP1 and PML. Yellow arrow: Area processed for 3D surface-rendering (Insets). E) FOXO4 and Ser15-phosphorylated p53, assessed as in 2A. Note that for FOXO4 a different antibody (Sigma) was used. F+G) Sequence (H indicates predicted helix) and 3D structure of FOXO4 used for the design of FOXO4-DRI. The amino acids indicated in yellow in F) are shown as yellow spheres in the displayed structure of FOXO4 (3L2C, protein databank). Green aa in F) are not visualized in this 3D structure, but are part of the FOXO4-DRI sequence. Red aa in G) change most upon p53-interaction (Wang et al., 2008). See also Fig. S2J-L. H) ¹H,¹⁵N HSQC NMR spectrum of ¹⁵N-labelled recombinant FOXO4⁸⁶⁻²⁰⁶ incubated with increasing stoichiometric equivalents of recombinant p53 (60, 120, 240 or 300 μ M, respectively). I) Experiment as in H), but with 1x or 2x stoichiometric equivalents of FOXO4-DRI (300 or 600 μ M, respectively). J) Cellular uptake of FOXO4-DRI in senescent IMR90 visualized by an antibody against the HIV-TAT sequence. K) Quantification of the

number of FOXO4/PML/53BP1-DNA-SCARS in control and senescent IMR90 incubated 3d with 25 μ M FOXO4-DRI and the pan Caspase-inhibitor QVD-OPH. # of small 53BP1 foci shown as control. Only infrequently FOXO4 foci were visible in control cells. L) Schematic representation of the p21^{Cip1} (CDKN1a) promoter in which the canonical FOXO target sequence is flanked by two p53 binding sites. M+N) Quantification of nuclear p21^{Cip1} intensity of senescent IMR90 treated as in K). N) Left: Immunoblot of senescent IMR90 cells incubated for the indicated time points with FOXO4-DRI and processed for Ser15-phosphorylated and total p53. Middle: Nuclear exclusion of pSer15-p53 in cell treated as in K+M). Right: Quantification of pSer15-p53 foci per nucleus of senescent IMR90.

Fig. 3: FOXO4-DRI selectively eliminates senescent cells through p53-mediated cell-intrinsic apoptosis

A) Viability assay of senescent and control IMR90 incubated with increasing doses of FOXO4-DRI (μ M). The selectivity index (SI50) reflects the differences in EC50 of a non-regression analysis for both groups. See also Fig. S3A. B) Real-time cell density measurement by xCELLigence of control and senescent IMR90 incubated with or without FOXO4-DRI (25 μ M). C) Viability assay comparing the effects of increasing doses of FOXO4-DRI and the same peptide in L-isofom, FOXO4-L. D) Viability assay comparing FOXO4-DRI, FOXO4-L, and an unrelated FOXM1-DRI peptide(Kruiswijk et al., 2016), at 6.25, 12.5 and 25 μ M, respectively. E) Viability assay comparing the pan-BCL inhibitor ABT-737 to FOXO4-DRI, when applied in three consecutive rounds at 1/3 the final concentration each (See also Fig. S3B+C). SI75 reflects differences in EC75 of a non-regression analysis for both groups. F) Viability assay comparing the effect of FOXO4-DRI on cells depleted for p53 by shRNA. See Fig. S3D for effects on p53 expression. G) Viability assay comparing the effect of FOXO4-DRI senescent cells incubated with pan-caspase inhibitors (20 μ M). H) Representative still images of real-time confocal-based imaging of senescent and control cells in the presence of a Caspase-3/7 activatable dye (green) and incubated with FOXO4-DRI. See also Mov. 3+4. Imaging started 8h after FOXO4-DRI addition.

Fig. 4: FOXO4-DRI counteracts Doxorubicin-induced senescence and chemotoxicity *in vivo*

A) SA- β -GAL assay to detect senescence in IMR90 7d after 2x treatment (1d in between) with 0.1 μ M Doxorubicin. B) Immunofluorescence for p16^{ink4a} and FOXO4 in control or Doxo-senescent IMR90. See also Fig. S4B. C) Quantification of the % of cells positive for p16^{ink4a}, IL1 α , IL6 and FOXO4 foci after Doxorubicin-induced senescence. D) Viability assay comparing the effect of FOXO4-DRI on control and Doxo-senescent cells *in vitro*. SI determined as in Fig. 3A. E) Viability assay comparing ABT-737 vs. FOXO4-DRI on Doxo-senescent cells. F) Same as in E, but both added 3x at 1/3 the final concentration. See also Fig. S4C. G) Viability assay comparing effects of incubation of FOXO4-DRI for various time points prior, during or after Doxorubicin exposure (blue line) vs. cells already induced to senesce by Doxorubicin (green boxes). M=Mock. H) Representative bioluminescence image and quantification of p16-driven senescence (RLUC) in p16::3MR mice (See Fig. S4A+D), treated as indicated with Doxorubicin, followed by FOXO4-DRI or Mock. I) Timeline of experiments in J-N. Doxorubicin: 2x i.p. at 10mg/kg. FOXO4-DRI: 3x i.v. at 5mg/kg, every other day (day 1, 3 and 5). J) Quantification of the % change in body weight of Doxorubicin-exposed mice treated with FOXO4-DRI or PBS, respectively. K) Quantification of the number of liver cells with ≥ 10 FOXO4 foci after Doxorubicin-exposure and treatment with PBS or FOXO4-DRI. L) Visualization and quantification of the % of liver cells from the mice in (K) expressing IL-6. M) Quantification of the Doxorubicin-induced increase in plasma AST levels as marker for liver damage. N) Quantification of the effects of PBS or FOXO4-DRI on Doxorubicin-induced plasma levels of AST and Urea as markers for liver and kidney damage, respectively. See also Fig. S4E+F.

Fig. 5: FOXO4-DRI decreases senescence and counters features of frailty in fast aging *Xpd*^{TTD/TTD} mice

A) Representative mice and quantification of p16^{ink4a}-driven RLUC Radiance in 26wk young wildtype and *Xpd*^{TTD/TTD} mice crossed into p16::3MR. B) Left: Timeline for visualization of effects of FOXO4-DRI or PBS on p16-driven senescence by bioluminescence in *Xpd*^{TTD/TTD}. Middle: Representative visualization of p16^{ink4a}-driven senescence in the same *Xpd*^{TTD/TTD}-p16::3MR mouse before and after FOXO4-DRI. Right: Quantification of the effects of FOXO4-DRI or PBS on senescence in a larger cohort of *Xpd*^{TTD/TTD}-p16::3MR mice. C) Timeline for measuring the effects of FOXO4-DRI or PBS on hair density, behavior and running wheel activity in D-I. D) FOXO4-DRI improves fur appearance of *Xpd*^{TTD/TTD} mice. Left panels:

Representative images of the same $Xpd^{TTD/TTD}$ animal before and after treatment with FOXO4-DRI. Right panel: quantification of the average change in fur score (See also Fig. S5A). E) Quantification of abdominal temperature measured by infrared thermometer as measure for fur density of wt vs. $Xpd^{TTD/TTD}$ mice (left) and the effects of FOXO4-DRI and PBS in the mice from D and Fig. S5A (right). F) Quantification of the response of the $Xpd^{TTD/TTD}$ mice from D to gentle physical stimuli before and after treatment with FOXO4-DRI or PBS. Note that $Xpd^{TTD/TTD}$ mice are generally relatively non-responsive. See also Fig. S5B. G) Quantification of the average distance run per day of wt. vs $Xpd^{TTD/TTD}$. H) Example of changes in running wheel behavior of a wt vs. $Xpd^{TTD/TTD}$ mouse treated with FOXO4-DRI. Data normalized to 100% for respective running wheel activity at baseline. On day 10 a blood sample was taken, resulting in a transient decrease in activity. I) Quantification of the average change in running wheel activity in wildtype and $Xpd^{TTD/TTD}$ mice after PBS or FOXO4-DRI treatment.

Fig. 6: By targeting senescence, FOXO4-DRI counters loss of renal function of $Xpd^{TTD/TTD}$ mice

A) Quantification of renal filtering capacity measured by plasma [Urea] in 13, 26 and 130w old wildtype mice and 13 and 26w $Xpd^{TTD/TTD}$ mice. B-D) Visualization of senescence (SA- β -GAL), the major SASP factor IL-6 and FOXO4 foci in 26w + 130w wildtype and 26w $Xpd^{TTD/TTD}$ old kidneys. Tubuli (T), Glomeruli (G). Inset C): Magnification of SA- β -GAL to reveal affected areas. Inset D) quantification of the % of renal cells expressing ≥ 10 FOXO4 foci. E) TUNEL assay to detect apoptosis in kidney sections of 130w old wt mice treated 3d with PBS or FOXO4-DRI. See Fig. S6A-D for pipeline and results with shFOXO4. F) Quantification of the % of platelets at time of sacrifice vs. baseline for wt and $Xpd^{TTD/TTD}$ mice treated with PBS or FOXO4-DRI. See also Fig. S6E. G) Representative Images of kidneys from 26w wt or $Xpd^{TTD/TTD}$ mice stained for LMNB1 loss. Quantified are the average number of nuclei per kidney positive for LMNB1 (at least 400 nuclei per mouse). H) Viability assay on control or senescent IMR90 incubated with recombinant IL1 α , IL1 β or IL1 receptor antagonist (IL1-RA) 24h prior to exposure of FOXO4-DRI. I) Viability plot showing the effect of FOXO4-DRI on control and senescent IMR90 pretreated with Cortisol and LPS, prior to FOXO4-DRI treatment. J) Staining as in G), but for the SASP marker IL-6. Quantified is the average IL-6 intensity per kidney over at least 3 frames per mouse for at least 4 mice per group. K) Quantification of the % plasma [Urea] of three pooled cohorts of wt and $Xpd^{TTD/TTD}$ mice (n=7-8 mice/treatment) after 30d

treatment with PBS or FOXO4-DRI. Data are represented as mean +/- SEM. See also Fig. S4G. L) Experiment as in K), but using Ganciclovir (GCV) to mediate semigenetic clearance of senescent cells through the Thymidine Kinase expressed by the p16::3MR construct. As GCV is i.p. administered, also FOXO4-DRI was i.p. administered in this experiment.

Fig. 7: By targeting senescence, FOXO4-DRI counters frailty and loss of renal function in naturally aged p16::3MR mice

A) Quantification of p16^{ink4a}-driven RLUC radiance in 104w old p13::3MR mice compared to 26w counterparts. Note there is a larger degree of spread in the signal, suggesting biological variation. B) Quantification of the % platelets at time of sacrifice/baseline of naturally aged p16::3MR mice treated with PBS or FOXO4-DRI for 30d. Procedure as in Fig. 5C. C) Representative images and quantification of p16^{ink4a}-driven RLUC radiance of mice the from B). D) Example of fur density in FOXO4-DRI vs. Mock-treated male p16::3MR mice. See also Fig. S7B. E) Quantification of the responsiveness of the mice in B-D treated with FOXO4-DRI or PBS. Analysis as in Fig. 5F. F-I) Quantification of the effects of FOXO4-DRI on LMNB1 loss and IL6 intensity in the kidneys and plasma [Urea] and [Creatinine] of the naturally aged p16::3MR mice from B). G) Quantification of % plasma [Urea] and [Creatinine] of naturally aged (110+wk) p16::3MR mice at 30d after i.p. injection with 3x 5mg/kg (every other day) FOXO4-DRI or 5x25mg/kg/day with GCV to clear senescent cells semigenetically.

STAR Methods

CONTACT FOR REAGENT AND RESOURCE SHARING

Further information and requests for resources and reagents should be directed to and will be fulfilled by the Lead Contact, Peter L.J. de Keizer (p.dekeizer@erasmusmc.nl). The following materials: $Xpd^{TTD/TTD}$ mice; p16::3MR mice and the peptide FOXO4-DRI are subject to patent applications and may be shared with research organizations for research and educational purposes only under an MTA to be discussed in good faith with the recipient; such MTA may restrict recipient to make any modifications to these materials.

EXPERIMENTAL MODEL AND SUBJECT DETAILS

Mouse experiments

This study was performed in strict accordance with all applicable federal and institutional policies. The protocol was approved by the Dutch Animal Ethics Committee. All the mice used in this study were of a C57BL/6J background; either wildtype, $Xpd^{TTD/TTD}$ mutated, expressing p16::3MR, or a combination thereof. The individual strains were backcrossed at least 10 times prior to this study. For the combination $Xpd^{TTD/TTD}$ x p16::3MR the F1 generation was used. The mice were used at the ages indicated in the figures, for Doxorubicin-experiments at 10-40wks of age, for $Xpd^{TTD/TTD}$ vs. wt experiments at 26-60 wks of age and for naturally aged mice at 115-130wks of age. All mice were kept in group housing until the start of the experiment after which they were placed in individual cages containing free access to a running wheel. Both sexes were used throughout the study. Where feasible, littermates of the same sex were used. These were randomly assigned to experimental groups.

Cell culture

The following cell lines were used in this study: IMR90 and WI-38 human fetal lung fibroblasts (female), BJ human foreskin fibroblasts (male), NIH3T3 mouse fibroblasts, wt and $bax/bak^{-/-}$ littermate Baby Mouse Kidney (BMK) cells, Human Embryonic Kidney (HEK) 293LTV. All cells were obtained from ATCC, except for wt and $bax/bak^{-/-}$ BMK cells which were a kind gift of Dr. Eileen White and have previously been

described(Degenhardt et al., 2002). All cells were maintained in high glucose Dulbecco's Modified Eagle's Medium (Lonza), supplemented with 10% Fetal Calf Serum, penicillin/streptomycin and 0.05% glutamine. IMR90, BJ, WI-38 cells were kept at 5% CO₂, 3% O₂ and used between 28-45 population doublings. The BMK cells were kept at 5% CO₂, 3% O₂. The NIH3T3 and HEK293LTV cells were maintained at 5% CO₂, ambient O₂. All cell lines were regularly tested for mycoplasma contamination using MycoAlert™ Mycoplasma Detection Kit (Lonza) and by assessment of (lack of) DAPI-positive microvesicles under fluorescence microscope. For IR-induced senescence, cells were exposed to 10Gy X- or Gamma rays, and analyzed 10 days later or otherwise indicated; control (proliferating) cells were mock irradiated, meaning they were taken out of the incubator and carried to the irradiator where they were placed outside for the same period of time as the irradiated cells. Senescence was confirmed by SA-β-GAL assay(Dimri et al., 1995) and/or changes in morphology. For Doxorubicin-induced senescence, the cells were treated twice with 0.1μM Doxorubicin (Sigma) with a 2d interval and analyzed 7d later, or as otherwise indicated.

Kidney slice culture

For tissue slice experiments, mice were used for which approval was obtained from the Committee on the Ethics of Animal Experiments of the Erasmus MC, where possible as a left-over from other experiments. Freshly isolated kidneys were sectioned in 200μM thick slices using a Vibratome (Leica, Eindhoven, the Netherlands). The sections were cultured in Dulbecco's modified eagle medium with 10% FCS at 37 °C, 5% CO₂ on a shaker (60 rpm). Following incubation with shRNA-containing lentiviral particles, or FOXO4-DRI, as indicated, the slices were fixed for 30min in formalin and stored at -80. Subsequently, they were subsectioned to 10μM slices using a Cryostat, placed on a charged microscopy slide and processed for TUNEL positivity.

METHOD DETAILS

Antibodies and reagents

Antibodies against the following proteins were used (See also Key Resource Table): Cell Signaling: FOXO1 (2880), FOXO4 (9472), Phospho-Ser15 p53 (9286), PUMA (4976), BIM (C3C5), Cleaved Caspase-3

(9661), Sigma: FOXO4 (HPA040232), Tubulin (clone B512; no: T5168), Abcam: BCL2 (Ab7972), IL6 (ab6672), Histone H3 (Ab1791-100), BD Transduction Laboratories: p21^{Cip1} (610234), BD Pharmigen: Cytochrome C (556432), R&D systems: IL1 α clone 4414, MAB200), human IL6 (AF206NA), Upstate: 53BP1 (05-726), Millipore: FOXO1 (07-702), Santa Cruz: p16^{Ink4a} (JC8; sc56330), PML (N19; sc9862), LMNB1 (M-20; sc-6217), Novacastra: mouse p53 (NCL-p53-CM55).

The following reagents were used: QVD-OPH (BD biosciences), ZVAD-FMK (SelleckChem), Rotenone (Sigma-Aldrich, St. Louis, MO, USA), Doxorubicin (Santa Cruz).

Lentivirus production and shRNAs

Lentiviruses were produced in an MLII-certified lab area, using the 3rd generation production system. In brief, HEK293LTV cells were transfected (Lipofectamine2000) with the packaging/envelope plasmids pRSV-Rev, pMDLg/pRRE and pMD2.G, in combination with a lentiviral transfer plasmid of choice. The next day, the media was refreshed. After 48h, the media was collected for transduction and stored at 4°C until needed. The following shRNA constructs were used (See also Key Resources Table): shGFP, shFOXO4-1: TRCN0000039720, Mature sequence: CCAGCTTCAGTCAGCAGTTAT, shFOXO4-2: TRCN0000039721, Mature sequence: CGTCCACGAAGCAGTTCAAAT, shFOXO4(mouse): TRCN0000071560, Mature sequence: GATCTGGATCTTGATATGTAT, shp53-1: TRCN0000003753, Mature sequence: CGGCGCACAGAGGAAGAGAAT and shp53-2: TRCN0000003754, Mature sequence: TCAGACCTATGGAACTACTT. For transient expression of FOXO1, we transfected cells with pBabe-Puro-FOXO1(de Keizer et al., 2010). For stable transduction of HRAS^{G12V}, we used pLENTI-Puro (670-1)-HRAS^{G12V}(Freund et al., 2012). The day after transduction, the cells were refreshed and 24h later placed on selection in media containing 0.5 μ g/ml puromycin. Three days later, the media was refreshed with media containing 1 μ g/ml puromycin in which they were kept throughout the assay. After 7d of selection, the cells were used in their respective assays. The shRNA-transduced cells were subsequently exposed to senescence-inducing IR and processed for Cell viability after 6d. For assays on IMR90 cells that were already senescent, treatment occurred as indicated (Fig. S1C) and the cells were subsequently processed for cell viability or cell density.

FOXO4 D-Retro-Inverso peptide development

FOXO4-DRI consists of the following amino acid sequence in D-Isoform:

H-Itrkepaseiaqsileaysqngwanrrsggkrpprrrrqrrkrg-OH. MW: 5358.2 It was manufactured by Pepscan (Lelystad, the Netherlands) at >95% purity and stored at -20°C in 1mg powder aliquots until used to avoid freeze-thawing artefacts. For *in vitro* experiments FOXO4-DRI was dissolved in PBS to generate a 2mM stock. For *in vivo* use, FOXO4-DRI was dissolved in PBS to generate a 5mg/ml stock solution, which was kept on ice until injection. Before injection the solution was brought to room temperature.

Total RNA isolation and mRNA sequencing sample preparation

The total RNA isolation and sequencing library preparation from IR-induced senescent and proliferating IMR90 cells was performed as follows: total RNA was isolated using Qiazol Lysis Reagent (Qiagen) and purified with the miRNeasy kit (Qiagen). The integrity (scores >9.0) of the RNA was determined on the Agilent 2100 Bioanalyzer (Agilent). Total RNA enrichment for sequencing poly(A) RNAs was performed with the TruSeq mRNA sample preparation kit (Illumina). 1µg of total RNA for each sample was used for poly(A) RNA selection using magnetic beads coated with poly-dT, followed by thermal fragmentation. The fragmented poly(A) RNA enriched samples were subjected to cDNA synthesis using Illumina TruSeq preparation kit. cDNA was synthesized by reverse transcriptase (Super-Script II) using poly-dT and random hexamer primers. The cDNA fragments were then blunt-ended through an end-repair reaction, followed by dA-tailing. Subsequently, specific double-stranded bar-coded adapters were ligated and library amplification for 15 cycles was performed. The pooled cDNA library consisted of equal concentration bar-coded samples. The pooled library was sequenced in one lane, 36 bp single read on the HiSeq2500 (Illumina). The analysis of the sequencing dataset was performed by Total RNA analysis pipeline (TRAP).

Total RNA analysis pipeline (TRAP)

Reads were aligned to the human hg19 reference genome using the NARWHAL automation software. Exonic reads were summed per transcript. A specific transcript was considered expressed, when a minimum number of reads, i.e. 5 reads per million, could be aligned to a transcript. Pathway analysis was performed with Ingenuity Pathway Analysis Software (IPA; Version build 242990).

Production and purification of recombinant proteins

The constructs corresponding to human FOXO4 (residues 86 – 206) and human p53 (residues 1 – 312), were purchased from Genscript in a pUC cloning vector. The DNA sequence was codon optimized for protein production in bacterial cells and flanked by NcoI and BamHI restriction sites. The coding region was cloned into a modified pETM-11 bacterial expression vector (EMBL Heidelberg) which was derived from a pET-24d(+) vector (Novagen) by insertion of a tobacco etch virus (TEV) protease cleavage site following a N terminal hexa-histidine and protein A tag. The genes were amplified by PCR using T4 primers (New England Biolabs). The resulting PCR products and pETM-11 were double digested with NcoI and BamHI enzymes (New England Biolabs) before ligation. The construct was verified by sequencing.

The human p53¹⁻³¹², and FOXO4⁸⁶⁻²⁰⁶ DNA sequences were codon optimized for protein production in bacterial cells and flanked by NcoI and BamHI restriction sites. The coding region was cloned into a modified pETM-11 bacterial expression vector which was derived from a pET-24d(+) vector (Novagen) by insertion of a tobacco etch virus (TEV) protease cleavage site following an N terminal hexa-histidine and protein A tag.

Unlabeled and uniformly (¹⁵N) labelled protein was produced in freshly transformed E. coli BL-21 (DE3) cells. A single colony was inoculated in Luria-Bertani medium (20 ml) with kanamycin (25 mg l⁻¹) and cultured at 37 °C overnight. From this, an aliquot (1 ml) was added to either 1 l unlabeled Luria-Bertani medium or 1 l ¹⁵N labelled M9 minimal medium (100 mM KH₂PO₄, 50 mM K₂HPO₄, 60 mM Na₂HPO₄, 14 mM K₂SO₄, 5 mM MgCl₂; pH 7.2 adjusted with HCl and NaOH with 0.1 dilution of trace element solution (41 mM CaCl₂, 22 mM FeSO₄, 6 mM MnCl₂, 3 mM CoCl₂, 1 mM ZnSO₄, 0.1 mM CuCl₂, 0.2 mM (NH₄)₆Mo₇O₂₄, 17 mM EDTA) with kanamycin (25 mg l⁻¹) in which ¹⁵N-NH₄Cl (2 g l⁻¹) was the only source of nitrogen for NMR isotope labelling purposes, respectively (Cambridge Isotope Laboratories, Inc). The culture was incubated at 37 °C and shaken at 200 rpm until the OD₆₀₀ reached 0.8. Protein expression was induced with 1 mM β-D-1-thiogalactopyranoside (IPTG) at 18 °C. The cells were pelleted after 20 hours by centrifugation using a Fiberlite F9-6x1000 rotor in a Sorvall LYNX 6000 Superspeed centrifuge at 2,000 g for 20 minutes, re-suspended in 40 ml lysis buffer containing 50 mM Tris, pH 7.5, 150 mM NaCl, 20 mM imidazole, 20 % glycerol, 2 mM TCEP, 250 units of Benzonase® Nuclease and bacterial Protease Inhibitor

Cocktail (Amresco; AEBSF, E-64, Bestatin, EDTA and Pepstatin) and were subsequently lysed by sonication. Lysates were cleared by centrifugation for 45 min at 4 °C (12 000 r.p.m.; Sorvall Lynx 6 000) and filtration (0.45 µm cellulose acetate syringe filters). Proteins were purified using Ni-NTA resins for immobilized metal affinity chromatography. Lysate was applied on the column and contaminants were removed using Wash buffer 1 (50 mM Tris, pH 7.5, 150 mM NaCl, 20 mM imidazole and 2 mM TCEP) and Wash buffer 2 (50 mM Tris, pH 7.5, 1 M NaCl, 20 mM imidazole and 2 mM TCEP). Protein was eluted (50 mM Tris, pH 7.5, 1 M NaCl, 500 mM imidazole and 2 mM TCEP) and the His6-Protein A tag was cleaved overnight at 4 °C using 2 (w/w) % of 1 mg/ml recombinant His-tagged TEV protease. The protein solution was buffer exchanged to Wash buffer 1 using HiPrep 26/10 Desalting column on an ÄKTA Pure system (GE Healthcare) at room temperature. Cleaved protein was repurified from the cleaved fusion tag and TEV protease by loading on a Ni-NTA resin column and 5 ml of the flow through was applied to a size-exclusion column (HiLoad Sepharose 16/600 75 µg, GE Healthcare) on an ÄKTA Pure system (GE Healthcare) at RT. The corresponding running buffer was composed of 50 mM sodium phosphate, pH 6.5, 150 mM NaCl and 1 mM DTT.

NMR spectroscopy

Samples for NMR measurements contained 300 µM ¹⁵N labeled FOXO4⁸⁶⁻²⁰⁶ protein in 50 mM sodium phosphate, pH 6.5, 150 mM NaCl and 1 mM DTT with 10% 2H₂O added for the lock signal. For NMR titrations, 0.2, 0.4, 0.8 and 1.0 stoichiometric equivalents of p53¹⁻³¹² (corresponding to 60, 120, 240 or 300 µM, respectively) and 1.0 and 2.0 stoichiometric equivalents of FOXO4-DRI (corresponding to 300 or 600 µM, respectively) were added. ¹H-¹⁵N HSQC NMR spectra were recorded at 298 K on a 700 MHz Bruker NMR spectrometer. All spectra were recorded with an interscan delay of 1.0 s, spectral widths of 15.9/30 ppm, centered at 4.7/118.0 ppm in ¹H/¹⁵N, with 1,024 and 256 points, respectively, and 16 scans per increment. NMR chemical shift assignments of FOXO4⁸⁶⁻²⁰⁶ were obtained from HNCACB and HNCA spectra using 500 µM of uniformly ¹⁵N,¹³C labeled protein in the aforementioned buffer at 298K on a 900 MHz Bruker Avance III NMR spectrometer equipped with a TCI cryoprobe.

Immunofluorescence and Structured Illumination Microscopy

Cells (typically 20,000) were grown on coverslips and after the indicated treatment fixed with formalin. Subsequently, cells were washed in Tris Buffered Saline (TBS) and permeabilized for 2-5 min in 2% Triton X-100 in TBS, depending on the antibody. Especially, the FOXO4 antibody (Cell Signaling) seemed to work better with shorter permeabilization times. To reduce background staining, the cells were quenched for 10min with 50nM glycine in TBS and blocked for 30min with 5% Normal Horse Serum (NHS) or Normal Goat Serum (NGS) in 0,2% gelatin-TBS solution, depending on the isotype of the secondary antibody. Subsequently, 30µl droplets containing primary antibody dilutions were placed on parafilm in a dark moisture chamber. The coverslips were placed facing the droplets and incubated overnight at 4°C. The next day, the coverslips were lifted by adding a small volume (~200µl) of TBS-Gelatine under the coverslip and transferred back to the 24-well plate. After washing 3x 20min with 1ml 0,2% gelatin-TBS secondary antibody incubation occurred as described for the primary antibody and the coverslips were incubated for one hour at room temperature. Following 3x 10min washes with 1ml 0,2% TBS-Gelatin and 1 wash with regular TBS the slides were mounted using soft set mounting medium with DAPI (Vectashield) and sealed with nail polish. Structured Illumination Microscopy was performed using a Zeiss Elyra PS1 microscope using a 63x 1.4 (n.a.) plan apo chromate oil immersion lens and 5 phases and 5 rotations of the illumination pattern. Intensity plots of individual pixels taken from a straight line in indicated immunofluorescence images were generated by twin slicer analysis using Huygens Professional 4.0 software (SVI, The Netherlands). Images were cropped and processed in Adobe Photoshop. When comparisons were made between images of the same experiment, all levels were adjusted equally and the ratio between the levels was not altered.

Quantitative real-time PCR

mRNA was extracted using the Cells-to-Ct kit (Ambion). QPCR was performed using the Universal Probe Library system (Roche) with the following primer/probe combinations (5'-3'), also listed in Table S1:

FOXO1 (NM_002015.3): Fwd: tggtttagaaaccaagtcc, Rev: ttggaccaagttcagttaca. UPL75

FOXO3 (NM_001455.3): Fwd: cagtagggcctgtgattcc, Rev: cagcagaccaacactgttcac. UPL73

FOXO4 (NM_005938.2): Fwd: acgagtggatgtccgtact, Rev: gtggcggatcgagttctc. UPL18

P21Cip1 (CDKN1A; NM_000389.3): Fwd: cgaagtcagttcctgtggag, Rev: catgggttctgacggacat. UPL82

ETS2 (NM_005239.4): Fwd: cagcgtcacctactgctctg, Rev: agtcgtgggtcttgggagtc. UPL27

Tubulin (NM_006009.2): Fwd: cttcgtctccgccatcag, Rev: ttgccaatctggacacca. UPL58

Immunoblotting

The dishes were washed 2x with ice-cold PBS, lysed in 1x Laemli sample buffer, and subjected to standard SDS-PAGE using separate 4%-12% Bis-Tris gels, after which the proteins were overnight transferred at 4°C to polyvinylidene fluoride membranes. The membranes were blocked using 2% BSA in Tris-buffered saline, 0.05% TWEEN (TBS-T) for 60min and incubated overnight at 4°C with the indicated primary antibodies. Following at least two 20min washing steps with TBS-T, the membranes were incubated with secondary antibodies for 60min. Following at least two 15min washing steps the membranes were developed with Enhanced Chemical Luminescence (Perkin Elmer). Images were cropped and equally processed in Adobe Photoshop.

Cell viability assays

The cells were plated in triplicate in 96-well plates (typically 7000 senescent and 2000 non-senescent cells). Unless otherwise indicated, cell viability was assessed 6d after plating, using the AQueousOne Solution Cell Proliferation Assay (Promega). 10 ul of CellTiter AQueousOne Solution in 100ul fresh culture medium was added to the wells before a 1-3 hour incubation at 37°C. Absorbance was measured at 490nm at a GloMax 96 well plate reader (Promega). A Mock-treated and a Puromycin (10µg/ml)-treated condition were used to set the maximal and minimal viability values, respectively, to which the experimental values were normalized.

Cell density assays

Stably transduced and Puromycin-selected IMR90 cells were plated in 24-well plates in triplicate. After 3d, cells were fixed in methanol and stained with 0.5% crystal violet in 25% methanol. The plates were dried, and cell density was quantified by destaining in 10% acetic acid and measuring absorbance of the solution at 560 nm.

Apoptosis assays

To assess apoptosis, two separate assays were used.

TUNEL staining was performed by permeabilizing cells fixed on coverslips for 2min with 0.1% Triton X-100 in 0.1% sodium citrate, followed by labeling with 10% TUNEL enzyme vs. label solution for 45min (Roche). Objective analysis of the percentage of TUNEL-positive cells was performed using CellProfiler software v2.3 by scoring the # of TUNEL positive objects filtered over DAPI-positive objects (Nuclei). Only TUNEL positive objects were considered that were also DAPI positive.

For the Cytochrome-C release assay, cells were seeded on coverslips in a 24-well plate and incubated for 5d total with the pan-caspase-inhibitor QVD-OPH (20 μ M in 500 μ l). The media was refreshed on day 3. Subsequently, the cells were processed for Cytochrome-C positivity by immunofluorescence. We measured the percentage of cells that showed a mitochondrial release of mitochondrial Cytochrome-C, identified either as diffuse staining, or complete absence.

Real-time cell density assay

Real-time cell density was measured using an xCELLigence detection system (ACEA Biosciences). Prior to the measurement, 50 μ L DMEM 10% FCS was added to each well of an E-plate view 16 (Roche) to establish background signal. Non-senescent (2000 cells per well) and senescent (5000 cells/well) IMR90 fibroblasts were then plated in 150 μ l medium. 16h later the E-plate was placed in the xCELLigence reader and the cell density was recorded every 30min. The cells were treated with 25 μ M FOXO4 peptide 8h after starting the measurements. Measurements continued for the indicated intervals.

Real-time imaging of Caspase-3/7 activation

Cells were plated in 4-well Poly-L-Lysine coated glass bottom 35mm dishes (D141410; Matsumi, Japan) and incubated with NucView488 Caspase-3 (4440; Essen Bioscience). FOXO4-DRI or PBS was added and the cells were transferred to a Heat and CO₂-controlled incubator, attached to a LSM510 confocal microscope (Zeiss). 8h after addition, real-time imaging was initiated and every 30min a grid of 3x3 pictures was recorded. The imaging continued for another 6 days and the images were concatenated using Zen imaging software (Zeiss; See Mov3+4).

Genotyping of mice

For PCR genotyping the following primers were used (See also Table S1):

For p16::3MR-1: p16::3MR1: 5'-AACGCAAACGCATGATCACTG-3' and

p16::3MR-2: 5'-TCAGGGATGATGCATCTAGC-3'. Positive animals show a band at 202bp.

For XpdTTD/TTD: p145: CCCGGCTAGAGTATCTGC, p184: GCCGGAATACGGGGCCA and

pβrev :TCTATGGTTAAGTTCATGTCATAGGAAGGGGAGAA.

Design of mouse experiments

For the calculation of the estimated sample size a power analysis was performed according to the formula: $n = 2(Z_{\alpha/2} + Z_{\beta})^2 * \sigma^2 / \Delta^2$, with a power (1-β) of 80% and a significance (α) of 0.05. Prior to the study, pilot experiments were performed to determine the differences in plasma [Urea] of 26wk old wt vs. *Xpd^{TTD/TTD}* mice. This led to a Δ and σ such that a sample size of 7 mice per group were estimated to be required to see differences in such experiments. This is shown in Fig. 6K. Later, it was found that sample sizes could be reduced when using mice of older age. This was applied in Fig. 6L and Fig. 7. For other assays, no information on Δ and σ was available and similar, or less stringent, sample sizes were deemed necessary. We only mice included mice that were of sufficient body weight at the start of the experiment, typically at least 80% of the average littermate weight of the same sex and genotype.

Assessment of running wheel activity

For assessment of running wheel behavior, we only included mice which at baseline ran at least 0.1km/day. Running wheel activity was continuously measured and plotted in km/day. The mice were placed in running wheel cages with ample time to adjust and get trained in using the wheel. After withdrawal of a blood sample, the mice were allowed to recover for at least 1 day and the average running wheel activity over the next two days was taken as baseline value. The mice were subsequently treated with FOXO4-DRI, or PBS (Mock) and at t=21d after baseline (t=18d after 1st treatment) the average running wheel activity over 4 days was scored. The ratio of mice of both sexes from four independent experiments was calculated and

the % activity plotted in Fig. 5I. Note that in some cases blood samples were taken at t=9 after treatment causing a temporary dip in activity.

Fur density analysis

Xpd^{TTD/TTD} mice show reduced fur density (de Boer et al., 2002; de Boer et al., 1998). To score any changes that might occur over time, the phenotype was ranged from 0-4 where 0 was very patched and 4 was wildtype. Each mouse was scored before and after the experiment as indicated in Fig. 5C and Fig. S5A. The final score was determined as the ratio (final-baseline)/baseline and the % change was subsequently plotted. Following several initial pilot observations, the experiment shown in Fig. 5C contains mice from two independent cohorts. For naturally aged mice (Fig. 7D), only males were included, since we did not observe significant hair loss in females. In these cohorts, 80% showed (varying degrees of) loss of hair at the beginning (115+wks), or developed it over the course of the experiment.

Infrared-measurements of abdominal temperature

From handling wt vs. *Xpd^{TTD/TTD}* mice, there appeared to be a difference in surface temperature. This we reasoned to be caused by changes in fur density. To further quantify such changes, the abdominal temperature was subsequently measured using an infrared thermometer. Even though the variation in individual measurements per animal was relatively large, *Xpd^{TTD/TTD}* mice showed a significantly higher average infrared-measured abdominal temperature in general (See also Fig. 5E). There were also mice with a relatively normal temperature. To assess the effect of FOXO4-DRI vs. PBS therefore only mice with a baseline temperature >34 degrees were included as the window of visualizing any changes would otherwise be too small.

Immunohistochemistry

For immunohistochemistry, paraffin sections of liver and intestine specimens were deparaffinized, rehydrated in decreasing concentrations of ethanol, treated for 10 minutes with 3% H₂O₂ to quench endogenous peroxidase activity and heated to 100°C for 1 h in 10 mM sodium citrate buffer, pH 6, for antigen retrieval. Subsequently the tissues were processed as for immunofluorescence. Paraffin embedded

heart tissue was serially sectioned into 5 μm slices, deparaffinized and rehydrated before Hematoxylin-Eosin (HE) staining or Picro Sirius Red staining was performed. For the HE staining, the sections were stained in Gills Hematoxylin (Sigma) for 4 minutes and 30 seconds in Eosin-Y solution. To stain for collagen, sections were incubated for 60 minutes in Picro Sirius Red solution (1g/L in picric acid) and briefly rinsed twice in 0.05% acetic acid.

Bioluminescence

For *in vivo* luminescence, mice were injected i.p. with 15 mg of Xenolight RediJect Coelenterazine (Caliper). 20 min later, the mice were anesthetized (2–4 % isoflurane) and placed in a dorsal position during imaging. Bioluminescence was measured with a Xenogen IVIS-200 Optical *in vivo* imaging System (Caliper Life Sciences; 5 min exposure). Photon flux was quantified within a circular region of interest (ROI) encompassing the site of substrate injection and the total radiance was corrected for time and surface area measured.

Plasma values as measure for tissue function

On the indicated time points, whole blood samples were collected in a Microvette with Lithium Heparin (Sarstedt) for plasma separation and spun for 10min at 4.6 x g. The (clear) supernatant was transferred into regular 1.5ml tubes and spun again for 5min at 4.6 x g. The supernatants were transferred again into 1.5ml tubes, snap frozen in liquid N₂ and stored at -80°C. [AST] was measured using an AST Activity Assay Kit (Sigma). The samples were incubated with 100 μl reaction mix in a 96 well plate and placed at 37°C. The absorbance at 450nm was determined after 2 minutes for baseline analysis and after 40 minutes for a final analysis. [Urea] was measured using a QuantiChrom Urea Assay Kit (Gentaur). The samples were incubated in 200 μl reaction mix for 10 minutes at room temperature before absorbance was measured at 520nm. [Creatinine] was measured using Creatinine Assay Kit (Sigma). Samples were incubated with 50 μl reaction mix at 37°C for 60 minutes and the absorbance was measured at 570nm. Ratios comparing plasma values after treatment compared to baseline were determined and plotted as % over baseline in scatter plots.

Post mortem SA- β -GAL assay

All tissues were flash frozen in Optimal Cutting Temperature (OCT) Tissue Tek and stored until ready for processing. Subsequently, 10 μ m slices were cryosectioned and placed on charged microscopy slides. These were washed with ice-cold PBS for 5min and fixed in formalin for 15min on ice. Immediately after fixation the samples were washed once briefly with MilliQ and stained overnight at 37°C with fresh SA- β -GAL solution (pH 6.0), containing 2,5 mM Na₂HPO₄, 7,4 mM Citric Acid, 0.15M NaCl, 2mM MgCl₂, 5 mM Potassium Ferricyanide, 5 mM Potassium Ferrocyanide and 25ul/ml 4% X-gal in DMF. Samples were mounted using soft set mounting medium with DAPI (Vectashield) and sealed with nail polish. Cultured cells were treated similarly.

QUANTIFICATION AND STATISTICAL ANALYSIS

Unpaired Student's t-tests were used to calculate the p value for pairwise comparisons. For multiple comparisons p-values were calculated using one-way ANOVA with Bonferroni post-test correction (Graph-Pad Prism). For comparisons of fold change differences an unpaired one-tailed t-test on the 2Log fold differences was applied. For the comparison of RLUC expression in naturally aged p16::3MR mice (Fig. 7A) and the change in abdominal temperature (Fig. 5E, right panel) a N-1 binary comparison test was performed. When averaging quantifications of single analyses, the "sum of squares"-rule was applied. The following indications of significance were used throughout the manuscript: * p<0.05, ** p<0.01.

DATA AND SOFTWARE AVAILABILITY

The RNA-Seq data obtained in this study has been uploaded to NCBI GEO datasets, under accession number GSE94395 (<https://www.ncbi.nlm.nih.gov/geo/query/acc.cgi?acc=GSE94395>).

The software to analyze the data is available at <http://rna-ome.erasmusmc.nl/>.

Supplemental Figure Legends

Figure S1. Related to Figure 1. A) Table showing color-coded changes in mRNA expression, fold change (F.C.) and p-values of the indicated apoptosis-associated genes in senescent vs. control IMR90. This figure is complementary to Fig. 1A showing the cell-intrinsic apoptosis pathway. B) Table showing the fold change and p-values of apoptosis-associated transcriptional regulators with FOXO4 highlighted in green. This figure complements Fig. 1B, which show a volcano plot of all transcriptional regulators. C) Treatment plan and visualization of cell density of senescent cells transduced with shRNAs against FOXO4. This figure is complementary to Fig. 1H).

Figure S2. Related to Figure 2. A) Quantification of the % of cells containing 3 or more FOXO4 foci after non-senescence inducing levels of gamma irradiation (0.5Gy and 2Gy) or senescence-inducing levels (10Gy) in time. B) Immunofluorescence of FOXO4 foci in and SA- β -GAL positive senescent cell. C) Immunofluorescence showing formation of foci, after 200nM Rotenone, 8J/m² UVC and Oncogene-induced senescence by stable ectopic expression of HRASG12V. D) Quantification of mouse NIH3T3 cells expressing 3 or more FOXO4 foci 7d after 10Gy IR, showing cross-species conservation of Foci formation. E+F) Visualization and quantification of the size of 53BP1, PML and FOXO4 foci in time after senescence induction, showing that 53BP1 foci and PML bodies expand, but FOXO4 foci remain the same in size. G-I) High magnification and pixel quantification of costainings between FOXO4 and PML (G), 53BP1 (H) and phosphorylated ATM-substrates (I) in nuclei of senescent IMR90. J+K) Heat-maps from two independent databases and independently scored (z-scored vs. non-z-scored), comparing FOXO1, 3 and 4 expression difference in various tissues. J) Z-scored mRNA expression profiles from Proteomicsdb(Wilhelm et al., 2014). K) Non-z-scored mRNA expression profiles from Proteinatlas(Uhlen et al., 2015). L) Sequence comparison of the sequence used for FOXO4-DRI revealing it to be identical in human and mouse FOXO4, but differs in 9 and 8 amino acids from FOXO1 and FOXO3a, respectively.

Figure S3. Related to Figure 3. A) Viability assay on control IMR90, BJ and WI-38 and counterparts induced to senesce by 10Gy IR, and incubated with FOXO4-DRI or PBS. B) Viability assays comparing the effects

of the cocktail of Quercetin (20 μ M) with increasing doses of Dasatinib, ABT-737 or FOXO4-DRI when applied once on control or senescent IMR90. C) Treatment schedule for Fig. 3E. D) Immunoblot determining the effect of two independent short hairpins against p53 on p53 expression. NIH3T3 cells were transiently transfected with the indicated shRNAs used in Fig. 3F in combination with pBABE-Puro. After 2d Puromycin selection the samples were processed for immunoblotting.

Figure S4. Related to Figure 4. A) Schematic overview of the p16::3MR construct, which comprises the promoter of p16ink4a that drives expression of a Trimodality reporter (3MR) consisting of Renilla Luciferase (RLUC) for bioluminescence detection, RFP for fluorescence detection and TK-HSV which can be used to induce selective clearance using Ganciclovir (GCV). B) Reduced, but subsequent doses of FOXO4-DRI, show to be more efficient in targeting Doxorubicin-senescent IMR90, than 1x high dose treatment. Senescent or Doxo-senescent IMR90 cells were exposed 1x to the final concentration of FOXO4-DRI, or 3x 1/3 that dose. The SI75 was compared between both treatment regimes. C) Immunofluorescence for IL6 in control or Doxo-senescent cells. D) Representative mice and quantification of p16-driven RLUC radiance in 5 mice i.p. injected with 10mg/kg Doxorubicin and analyzed on the indicated time-points. E) Visualization of change in Doxorubicin-induced p16-mediated senescence through bioluminescence in mice treated as in Fig. 4I, but with 5x 25mg/kg i.p GCV (day 1,2,3,4,5) for semigenetic clearance of senescence, or the same regimen in addition to 3x i.v. 5mg/kg FOXO4-DRI (day 1,3,5). F) Quantification of the % AST in plasma of mice from Fig. S4E after treatment vs. baseline.

Figure S5. Related to Figure 5. A) Overview of the fur status of the indicated XpdTTD/TTD mice before or after treatment with PBS (Left columns) or FOXO4-DRI (Right columns), respectively. The mice were scored 0-4 where 4 is fur as seen in wildtype mice and 0 is most reduced. The % change was calculated for each mouse and plotted in Fig. 5D. Red arrows indicate deterioration of the indicated area over time, whereas green arrows indicate improvement. B) Example of difference in behavior of XpdTTD/TTD mice treated with PBS, or FOXO4-DRI. To address this more quantitatively, the responsiveness to gentle stimuli was measured as described in Fig. 5F.

Figure S6. Related to Figure 6. A) Schematic overview of kidney slice culture experiment and subsequent analysis. Fresh kidneys were isolated and sectioned in 200 μ M slices. These were placed in 24-well plate wells in tissue culture medium while rotating at 60rpm (See also(Kruiswijk et al., 2016)). Following treatment with shRNAs the slices were processed for TUNEL staining and the percentage positive cells is objectively scored. B) Treatment plan for kidney slice experiments in Fig. 6E and Fig. S6C-D. C) Example of shGFP and shFOXO4 (mouse) transduced 130w WT kidney slices stained for TUNEL (left), segmented for DAPI (middle) and scored for percentage TUNEL positive (right) using Cellprofiler V2.3. D) Quantification of n=6 kidney slices processed as in C). E) Whole blood analysis of the mice in Fig. 6F. F) Heart sections of PBS, or FOXO4-DRI treated wt mice (26w), stained by H&E for general pathology, and Picro Sirius Red to visualize collagen deposition. N>4. No apparent abnormalities were observed. G) FOXO4-DRI does not significantly alter total body weight, nor kidney weight (normalized to total body weight) of WT or XpdTTD/TTD mice. This figure complements Fig. 6G, J, K and L, by showing that while FOXO4-DRI does not influence total kidney mass it does improve renal function.

Figure S7. Related to Figure 7. A) Quantitative representation of the % p16-driven senescence (RLUC) in naturally aged mice treated with FOXO4-DRI or PBS. Note the large biological spread in signal. B) Overview of the fur status of the indicated naturally aged mice before or after treatment with PBS (Left columns) or FOXO4-DRI (Right columns), respectively. Right panel: quantification of the % change as also described in Fig. 5D. C) Quantification of the % change in body weight of naturally aged mice treated as in Fig. 7B-I (Left panel), or Fig. 7J (Right panel).

Mov. 1. Related to Fig. 2D. Structured Illumination Microscopic (SIM) image of the nucleus of a senescent IMR90 cell.

Senescent IMR90 cells were stained for FOXO4 (Alexa488; Green), 53BP1 (Alexa594; Red) and PML (Alexa647; Purple) and DAPI (Blue). A SIM image was taken and this movie shows the combinations of the respective colors of a representative image. See also Mov. 2.

Mov. 2. Related to Fig. 2D. 3D reconstruction of a representative FOXO4/53BP1/PML cluster in the nucleus of a senescent IMR90 cell.

Senescent IMR90 cells were stained for FOXO4 (Alexa488; Green), 53BP1 (Alexa594; Red) and PML (Alexa647; Purple) and DAPI (Blue). A SIM image was taken and the focal structure indicated by the yellow line in Fig. 2D was processed for 3D reconstruction, using Amira software. See also Mov. 1.

Mov. 3. Related to Fig. 3H. Lack of Caspase-3 activity in control IMR90 cells incubated with FOXO4-DRI. Control IMR90 cells were incubated with a dye that turns green upon activation of Caspase-3 (NucView488 Caspase-3) and 25 μ M FOXO4-DRI. After 8h the cells were processed for real-time imaging for 6 days in total. See also Mov. 4

Mov. 4. Related to Fig. 3H. Induction of Caspase-3 activity in senescent IMR90 cells incubated with FOXO4-DRI.

IR-senescent IMR90 cells were incubated with a dye that turns green upon activation of Caspase-3 (NucView488 Caspase-3) and 25 μ M FOXO4-DRI. After 8h the cells were processed for real-time imaging for 6 days in total. See also Mov. 3.

References

Baker, D.J., Childs, B.G., Durik, M., Wijers, M.E., Sieben, C.J., Zhong, J., Saltness, R.A., Jeganathan, K.B., Verzosa, G.C., Pezeshki, A., *et al.* (2016). Naturally occurring p16(Ink4a)-positive cells shorten healthy lifespan. *Nature* 530, 184-189.

Beydoun, T., Deloche, C., Perino, J., Kirwan, B.A., Combette, J.M., and Behar-Cohen, F. (2015). Subconjunctival injection of XG-102, a JNK inhibitor peptide, in patients with intraocular inflammation: a safety and tolerability study. *J Ocul Pharmacol Ther* 31, 93-99.

Borsello, T., Clarke, P.G., Hirt, L., Vercelli, A., Repici, M., Schorderet, D.F., Bogousslavsky, J., and Bonny, C. (2003). A peptide inhibitor of c-Jun N-terminal kinase protects against excitotoxicity and cerebral ischemia. *Nat Med* 9, 1180-1186.

Botter, S.M., Zar, M., van Osch, G.J., van Steeg, H., Dolle, M.E., Hoeijmakers, J.H., Weinans, H., and van Leeuwen, J.P. (2011). Analysis of osteoarthritis in a mouse model of the progeroid human DNA repair syndrome trichothiodystrophy. *Age (Dordr)* 33, 247-260.

Brown, J.P., Wei, W., and Sedivy, J.M. (1997). Bypass of senescence after disruption of p21CIP1/WAF1 gene in normal diploid human fibroblasts. *Science* 277, 831-834.

Cahu, J., Bustany, S., and Sola, B. (2012). Senescence-associated secretory phenotype favors the emergence of cancer stem-like cells. *Cell Death Dis* 3, e446.

Campisi, J. (2013). Aging, cellular senescence, and cancer. *Annu Rev Physiol* 75, 685-705.

Chang, J., Wang, Y., Shao, L., Laberge, R.M., Demaria, M., Campisi, J., Janakiraman, K., Sharpless, N.E., Ding, S., Feng, W., *et al.* (2016). Clearance of senescent cells by ABT263 rejuvenates aged hematopoietic stem cells in mice. *Nature medicine* 22, 78-83.

Coppe, J.P., Patil, C.K., Rodier, F., Sun, Y., Munoz, D.P., Goldstein, J., Nelson, P.S., Desprez, P.Y., and Campisi, J. (2008). Senescence-associated secretory phenotypes reveal cell-nonautonomous functions of oncogenic RAS and the p53 tumor suppressor. *PLoS Biol* 6, 2853-2868.

Damodar, G., Smitha, T., Gopinath, S., Vijayakumar, S., and Rao, Y. (2014). An evaluation of hepatotoxicity in breast cancer patients receiving injection Doxorubicin. *Ann Med Health Sci Res* 4, 74-79.

de Boer, J., Andressoo, J.O., de Wit, J., Huijmans, J., Beems, R.B., van Steeg, H., Weeda, G., van der Horst, G.T., van Leeuwen, W., Themmen, A.P., *et al.* (2002). Premature aging in mice deficient in DNA repair and transcription. *Science* 296, 1276-1279.

de Boer, J., de Wit, J., van Steeg, H., Berg, R.J., Morreau, H., Visser, P., Lehmann, A.R., Duran, M., Hoeijmakers, J.H., and Weeda, G. (1998). A mouse model for the basal transcription/DNA repair syndrome trichothiodystrophy. *Mol Cell* 1, 981-990.

de Keizer, P.L. (2017). The Fountain of Youth by Targeting Senescent Cells? *Trends Mol Med* 23, 6-17.

de Keizer, P.L., Burgering, B.M., and Dansen, T.B. (2011). Forkhead box o as a sensor, mediator, and regulator of redox signaling. *Antioxidants & redox signaling* 14, 1093-1106.

de Keizer, P.L., Packer, L.M., Szybowska, A.A., Riedl-Polderman, P.E., van den Broek, N.J., de Bruin, A., Dansen, T.B., Marais, R., Brenkman, A.B., and Burgering, B.M. (2010). Activation of forkhead box O

transcription factors by oncogenic BRAF promotes p21cip1-dependent senescence. *Cancer research* 70, 8526-8536.

Degenhardt, K., Sundararajan, R., Lindsten, T., Thompson, C., and White, E. (2002). Bax and Bak independently promote cytochrome C release from mitochondria. *The Journal of biological chemistry* 277, 14127-14134.

Deloche, C., Lopez-Lazaro, L., Mouz, S., Perino, J., Abadie, C., and Combette, J.M. (2014). XG-102 administered to healthy male volunteers as a single intravenous infusion: a randomized, double-blind, placebo-controlled, dose-escalating study. *Pharmacol Res Perspect* 2, e00020.

Demaria, M., Ohtani, N., Youssef, S.A., Rodier, F., Toussaint, W., Mitchell, J.R., Laberge, R.M., Vijg, J., Van Steeg, H., Dolle, M.E., *et al.* (2014). An essential role for senescent cells in optimal wound healing through secretion of PDGF-AA. *Dev Cell* 31, 722-733.

Di, L.A., Linke, S.P., Clarkin, K., and Wahl, G.M. (1994). DNA damage triggers a prolonged p53-dependent G1 arrest and long-term induction of Cip1 in normal human fibroblasts. *Genes Dev* 8, 2540-2551.

Dimri, G.P., Lee, X., Basile, G., Acosta, M., Scott, G., Roskelley, C., Medrano, E.E., Linskens, M., Rubelj, I., and Pereira-Smith, O. (1995). A biomarker that identifies senescent human cells in culture and in aging skin in vivo. *ProcNatlAcadSciUSA* 92, 9363-9367.

Eijkelenboom, A., and Burgering, B.M. (2013). FOXOs: signalling integrators for homeostasis maintenance. *Nat Rev Mol Cell Biol* 14, 83-97.

Ewald, J.A., Desotelle, J.A., Wilding, G., and Jarrard, D.F. (2010). Therapy-induced senescence in cancer. *J Natl Cancer Inst* 102, 1536-1546.

Ferrucci, L., Corsi, A., Lauretani, F., Bandinelli, S., Bartali, B., Taub, D.D., Guralnik, J.M., and Longo, D.L. (2005). The origins of age-related proinflammatory state. *Blood* 105, 2294-2299.

Freund, A., Laberge, R.M., Demaria, M., and Campisi, J. (2012). Lamin B1 loss is a senescence-associated biomarker. *Mol Biol Cell* 23, 2066-2075.

Freund, A., Patil, C.K., and Campisi, J. (2011). p38MAPK is a novel DNA damage response-independent regulator of the senescence-associated secretory phenotype. *EMBO J* 30, 1536-1548.

Gowda, S., Desai, P.B., Kulkarni, S.S., Hull, V.V., Math, A.A., and Vernekar, S.N. (2010). Markers of renal function tests. *N Am J Med Sci* 2, 170-173.

Guichard, G., Benkirane, N., Zeder-Lutz, G., van Regenmortel, M.H., Briand, J.P., and Muller, S. (1994). Antigenic mimicry of natural L-peptides with retro-inverso-peptidomimetics. *Proceedings of the National Academy of Sciences of the United States of America* *91*, 9765-9769.

Henderson, T.O., Ness, K.K., and Cohen, H.J. (2014). Accelerated aging among cancer survivors: from pediatrics to geriatrics. *Am Soc Clin Oncol Educ Book*, e423-430.

Herce, H.D., and Garcia, A.E. (2007). Molecular dynamics simulations suggest a mechanism for translocation of the HIV-1 TAT peptide across lipid membranes. *Proceedings of the National Academy of Sciences of the United States of America* *104*, 20805-20810.

Hoeijmakers, J.H. (2009). DNA damage, aging, and cancer. *N Engl J Med* *361*, 1475-1485.

Hosaka, T., Biggs, W.H., 3rd, Tieu, D., Boyer, A.D., Varki, N.M., Cavenee, W.K., and Arden, K.C. (2004). Disruption of forkhead transcription factor (FOXO) family members in mice reveals their functional diversification. *Proc Natl Acad Sci U S A* *101*, 2975-2980.

Krishnamurthy, J., Torrice, C., Ramsey, M.R., Kovalev, G.I., Al-Regaiey, K., Su, L., and Sharpless, N.E. (2004). Ink4a/Arf expression is a biomarker of aging. *J Clin Invest* *114*, 1299-1307.

Kruiswijk, F., Hasenfuss, S.C., Sivapatham, R., Baar, M.P., Putavet, D., Naipal, K.A., van den Broek, N.J., Kruit, W., van der Spek, P.J., van Gent, D.C., *et al.* (2016). Targeted inhibition of metastatic melanoma through interference with Pin1-FOXM1 signaling. *Oncogene* *35*, 2166-2177.

Kruiswijk, F., Labuschagne, C.F., and Vousden, K.H. (2015). p53 in survival, death and metabolic health: a lifeguard with a licence to kill. *Nat Rev Mol Cell Biol* *16*, 393-405.

Lopez-Otin, C., Blasco, M.A., Partridge, L., Serrano, M., and Kroemer, G. (2013). The hallmarks of aging. *Cell* *153*, 1194-1217.

Lyman, J.L. (1986). Blood urea nitrogen and creatinine. *Emerg Med Clin North Am* *4*, 223-233.

Martins, R., Lithgow, G.J., and Link, W. (2016). Long live FOXO: unraveling the role of FOXO proteins in aging and longevity. *Aging Cell* *15*, 196-207.

Mihara, M., Erster, S., Zaika, A., Petrenko, O., Chittenden, T., Pancoska, P., and Moll, U.M. (2003). p53 has a direct apoptogenic role at the mitochondria. *Molecular cell* *11*, 577-590.

Munoz-Espin, D., Canamero, M., Maraver, A., Gomez-Lopez, G., Contreras, J., Murillo-Cuesta, S., Rodriguez-Baeza, A., Varela-Nieto, I., Ruberte, J., Collado, M., *et al.* (2013). Programmed cell senescence during mammalian embryonic development. *Cell* 155, 1104-1118.

Nakae, J., Kitamura, T., Kitamura, Y., Biggs, W.H., 3rd, Arden, K.C., and Accili, D. (2003). The forkhead transcription factor Foxo1 regulates adipocyte differentiation. *Dev Cell* 4, 119-129.

Orjalo, A.V., Bhaumik, D., Gengler, B.K., Scott, G.K., and Campisi, J. (2009). Cell surface-bound IL-1alpha is an upstream regulator of the senescence-associated IL-6/IL-8 cytokine network. *Proceedings of the National Academy of Sciences of the United States of America* 106, 17031-17036.

Paik, J.H., Kollipara, R., Chu, G., Ji, H., Xiao, Y., Ding, Z., Miao, L., Tothova, Z., Horner, J.W., Carrasco, D.R., *et al.* (2007). FoxOs are lineage-restricted redundant tumor suppressors and regulate endothelial cell homeostasis. *Cell* 128, 309-323.

Renault, V.M., Rafalski, V.A., Morgan, A.A., Salih, D.A., Brett, J.O., Webb, A.E., Villeda, S.A., Thekkat, P.U., Guillerrey, C., Denko, N.C., *et al.* (2009). FoxO3 regulates neural stem cell homeostasis. *Cell Stem Cell* 5, 527-539.

Rodier, F., Coppe, J.P., Patil, C.K., Hoeijmakers, W.A., Munoz, D.P., Raza, S.R., Freund, A., Campeau, E., Davalos, A.R., and Campisi, J. (2009). Persistent DNA damage signalling triggers senescence-associated inflammatory cytokine secretion. *Nat Cell Biol* 11, 973-979.

Rodier, F., Munoz, D.P., Teachenor, R., Chu, V., Le, O., Bhaumik, D., Coppe, J.P., Campeau, E., Beausejour, C.M., Kim, S.H., *et al.* (2011). DNA-SCARS: distinct nuclear structures that sustain damage-induced senescence growth arrest and inflammatory cytokine secretion. *J Cell Sci* 124, 68-81.

Roninson, I.B. (2003). Tumor cell senescence in cancer treatment. *Cancer research* 63, 2705-2715.

Schoenwaelder, S.M., Jarman, K.E., Gardiner, E.E., Hua, M., Qiao, J., White, M.J., Josefsson, E.C., Alwis, I., Ono, A., Willcox, A., *et al.* (2011). Bcl-xL-inhibitory BH3 mimetics can induce a transient thrombocytopathy that undermines the hemostatic function of platelets. *Blood* 118, 1663-1674.

Suckfuell, M., Lisowska, G., Domka, W., Kabacinska, A., Morawski, K., Bodlaj, R., Klimak, P., Kostrica, R., and Meyer, T. (2014). Efficacy and safety of AM-111 in the treatment of acute sensorineural hearing loss: a double-blind, randomized, placebo-controlled phase II study. *Otol Neurotol* 35, 1317-1326.

Tait, S.W., and Green, D.R. (2010). Mitochondria and cell death: outer membrane permeabilization and beyond. *Nat Rev Mol Cell Biol* 11, 621-632.

Vaupel, J.W. (2010). Biodemography of human ageing. *Nature* 464, 536-542.

Wang, E. (1995). Senescent human fibroblasts resist programmed cell death, and failure to suppress bcl2 is involved. *Cancer research* 55, 2284-2292.

Wang, F., Marshall, C.B., Yamamoto, K., Li, G.Y., Plevin, M.J., You, H., Mak, T.W., and Ikura, M. (2008). Biochemical and structural characterization of an intramolecular interaction in FOXO3a and its binding with p53. *J Mol Biol* 384, 590-603.

Warso, M.A., Richards, J.M., Mehta, D., Christov, K., Schaeffer, C., Rae Bressler, L., Yamada, T., Majumdar, D., Kennedy, S.A., Beattie, C.W., *et al.* (2013). A first-in-class, first-in-human, phase I trial of p28, a non-HDM2-mediated peptide inhibitor of p53 ubiquitination in patients with advanced solid tumours. *British journal of cancer* 108, 1061-1070.

Wijnhoven, S.W., Beems, R.B., Roodbergen, M., van den Berg, J., Lohman, P.H., Diderich, K., van der Horst, G.T., Vijg, J., Hoeijmakers, J.H., and van Steeg, H. (2005). Accelerated aging pathology in ad libitum fed Xpd(TTD) mice is accompanied by features suggestive of caloric restriction. *DNA repair* 4, 1314-1324.

Xu, M., Tchkonja, T., Ding, H., Ogrodnik, M., Lubbers, E.R., Pirtskhalava, T., White, T.A., Johnson, K.O., Stout, M.B., Mezera, V., *et al.* (2015). JAK inhibition alleviates the cellular senescence-associated secretory phenotype and frailty in old age. *Proceedings of the National Academy of Sciences of the United States of America* 112, E6301-6310.

Yosef, R., Pilpel, N., Tokarsky-Amiel, R., Biran, A., Ovadya, Y., Cohen, S., Vadai, E., Dassa, L., Shahar, E., Condiotti, R., *et al.* (2016). Directed elimination of senescent cells by inhibition of BCL-W and BCL-XL. *Nat Commun* 7, 11190.

Zhou, W., Cao, Q., Peng, Y., Zhang, Q.J., Castrillon, D.H., DePinho, R.A., and Liu, Z.P. (2009). FoxO4 inhibits NF-kappaB and protects mice against colonic injury and inflammation. *Gastroenterology* 137, 1403-1414.

Zhu, Y., Tchkonja, T., Pirtskhalava, T., Gower, A.C., Ding, H., Giorgadze, N., Palmer, A.K., Ikeno, Y., Hubbard, G.B., Lenburg, M., *et al.* (2015). The Achilles' heel of senescent cells: from transcriptome to senolytic drugs. *Aging Cell* 14, 644-658.

KEY RESOURCES TABLE

REAGENT or RESOURCE	SOURCE	IDENTIFIER
Antibodies		
Mouse monoclonal anti-53BP1	Millipore	Cat#05-726
Mouse monoclonal anti-BCL2	Abcam	Cat#Ab7972
Rabbit monoclonal anti-BIM	Cell signaling	Cat#C3C5
Rabbit polyclonal anti-Cleaved Caspase-3	Cell signaling	Cat#9661
Mouse monoclonal anti-Cytochrome C	BD Pharmigen	Cat#556432
Rabbit monoclonal anti-FOXO1	Cell signaling	Cat#2880
Rabbit polyclonal anti-FOXO1	Millipore	Cat#07-702
Rabbit polyclonal anti-FOXO4	Cell signaling	Cat#9472
Rabbit polyclonal anti-FOXO4	Sigma	Cat#HPA040232
Rabbit polyclonal anti-Histone H3	Abcam	Cat#ab1791-100
Mouse monoclonal anti-HIV1 TAT	Abcam	Cat#ab63957
Mouse monoclonal anti-IL1 α clone 4414	R&D systems	Cat#MAB200
Rabbit polyclonal anti-IL6	Abcam	Cat#ab6672
Goat polyclonal anti-IL6	R&D systems	Cat#AF206NA
Rabbit polyclonal anti-LMNB1	Abcam	Cat#ab16048
Mouse monoclonal anti-p16Ink4a clone JC8	Santa Cruz	Cat#sc56330
Mouse monoclonal anti-p21Cip1	BD Transduction Laboratories	Cat#610234
Rabbit polyclonal anti-p53	Novacastra	Cat#NCL-p53-CM55
Mouse monoclonal anti-phospho-Ser15 p53	Cell signaling	Cat#9286
Goat polyclonal anti-PML N19	Santa Cruz	Cat#sc9862
Rabbit polyclonal anti-PUMA	Cell signaling	Cat#4976
Mouse monoclonal anti-Tubulin clone B512	Sigma	Cat#T5168
Donkey anti-Goat 594	Thermo Fischer	Cat#A-11058
Donkey anti-Goat 647	Thermo Fisher	Cat#A-21447
Donkey anti-Mouse 488	Thermo Fischer	Cat#A-21202
Donkey anti-Mouse 594	Thermo Fischer	Cat#A-21203
Donkey anti-Rabbit 488	Thermo Fischer	Cat#A-21206
Donkey anti-Rabbit 594	Thermo Fischer	Cat#A-21207
Donkey anti-Mouse HRP	Dako	Cat#P0161
Donkey anti-Rabbit HRP	Dako	Cat#P0448
Bacterial and Virus Strains		
E.coli BL21 (DE3)	Agilent Technologies	CAT#: 200131 Lot#: 0006276950
Chemicals, Peptides, and Recombinant Proteins		
Benzonase® Nuclease	Sigma Aldrich	CAS#: E1014 Lot#: SLBM6125V
Doxorubicin	Santa Cruz	Cat#sc-200923A
FOXO4 D-Retro-Inverso peptide H-Itlrkepaseiaqsileaysqngwanrrsggkrpppprrrqrkkrg-OH	This paper, manufactured by Pepscan	N/A
NucView488 Caspase-3	Essen Bioscience	Cat#4440
QVD-OPH	BD biosciences	Cat#03OPH10905
Rotenone	Sigma-Aldrich	Cat#R8875
VECTASHIELD Antifade Mounting Medium with DAPI	Vector Laboratories	Cat# H1200
Xenolight RediJect Coelentarazine	Caliper	Cat#770505
ZVAD-FMK	R&D systems	Cat#FMK001

Critical Commercial Assays		
AST Activity Assay Kit	Sigma	Cat#MAK055
Aqueous One Solution Cell Proliferation Assay	Promega	Cat#G3582
Creatinine assay kit	Sigma	Cat#MAK080
In Situ Cell Death Detection Kit	Roche	Cat#11684795910
miRNeasy mini kit	Qiagen	Cat#217004
QuantiChrom Urea Assay Kit	Gentaur	Cat#DIUR-500
TruSeq mRNA sample preparation kit	Illumina	Cat#RS-122-2101
Deposited Data		
RNA sequencing data	This study	GSE94395
Experimental Models: Cell Lines		
BJ	ATCC	Cat#CRL-2522
BMK cells, wt and <i>Bax/Bak</i> ^{-/-}	Gift from Dr. Eileen White. (Degenhardt et al., 2002)	N/A
HEK293LTV	ATCC	Cat#CRL-1573
IMR90	ATCC	Cat#CCL-186
NIH3T3	ATCC	Cat#CRL-1658
WI-38	ATCC	Cat#CCL-75
Experimental Models: Organisms/Strains		
Mouse: C57BL/6J	(de Boer et al., 1998)	N/A
Mouse: C57BL/6J p16::3MR	(Demaria et al., 2014)	N/A
Mouse: C57BL/6J <i>Xpd</i> ^{TTD/TTD}	(de Boer et al., 1998)	N/A
Oligonucleotides		
Primers for QPCR and genotyping, see table S1		
shFOXO4-1 CCAGCTTCAGTCAGCAGTTAT	GPP	TRCN0000039720
shFOXO4-2 CGTCCACGAAGCAGTTCAAAT	GPP	TRCN0000039721
shFOXO4(mouse) GATCTGGATCTTGATATGTAT	GPP	TRCN0000071560
shp53-1 CGGCGCACAGAGGAAGAGAAT	GPP	TRCN0000003753
shp53-2 CGGCGCACAGAGGAAGAGAAT	GPP	TRCN0000003754
Recombinant DNA		
pETM-11	EMBL Heidelberg	N/A
pUC-FOXO4 ⁸⁶⁻²⁰⁶	GenScript	N/A
pUC-p53 ¹⁻³¹²	GenScript	N/A
Software and Algorithms		
CcpNmr 2.4.2	CCPN	http://www.ccpn.ac.uk/v2-software/downloads/stable
Ingenuity Pathway Analysis Software, version build 242990	Qiagen	https://www.qiagenbioinformatics.com/products/ingenuity-pathway-analysis/

TopSpinTM 3.1	Bruker	https://www.bruker.com/products/mr/nmr/nmr-software/software.html
TRAP	ErasmusMC	http://rna-ome.erasmusmc.nl/
<u>Other</u>		
Ammonium chloride (15N, 99%)	Cambridge Isotope Laboratories, Inc	CAS#: 12125-02-9 Lot#: 13K-451
D-Glucose (U- ¹³ C ₆ , 99%)	Cambridge Isotope Laboratories, Inc	CAS#: 110187—42-3 Lot#: PR-26833
Deuterium oxide (99.9 atom %D)	Sigma Aldrich	CAS#: 7789-20-0 Lot#: STBF0098V

Table S1. List of oligonucleotides		
<u>Name</u>	<u>Sequence</u>	<u>Note</u>
FOXO1 forward primer	TGGTTTTAGAAACCCAAGTTCC	QPCR (with UPL75)
FOXO1 reverse primer	TTGGCACCAAGTTCAGTTACA	QPCR (with UPL75)
FOXO3 forward primer	CAGTAGGGCCTGTGATTTCC	QPCR (with UPL73)
FOXO3 reverse primer	GTGGCGGATCGAGTTCTTC	QPCR (with UPL73)
FOXO4 forward primer	ACGAGTGGATGGTCCGTA CT	QPCR (with UPL18)
FOXO4 reverse primer	GTGGCGGATCGAGTTCTTC	QPCR (with UPL18)
CDKN1A forward primer	CGAAGTCAGTTCCTTGTGGAG	QPCR (with UPL82)
CDKN1A reverse primer	AGTCGTGGTCTTTGGGAGTC	QPCR (with UPL82)
ETS2 forward primer	CAGCGTCACCTACTGCTCTG	QPCR (with UPL27)
ETS2 reverse primer	AGTCGTGGTCTTTGGGAGTC	QPCR (with UPL27)
Tubulin forward primer	CTTCGTCTCCGCCATCAG	QPCR (with UPL58)
Tubulin reverse primer	TTGCCAATCTGGACACCA	QPCR (with UPL58)
p16::3MR forward primer	AACGCAAACGCATGATCACTG	Genotyping
p16::3MR Reverse primer	TCAGGGATGATGCATCTAGC	Genotyping
XpdTTD/TTD p145	CCCGGCTAGAGTATCTGC	Genotyping
XpdTTD/TTD p184	GCCGGAATACGGGGCCA	Genotyping
XpdTTD/TTD pβrev	TCTATGGTTAAGTTCATGTCATAGGAAGGGGA GAA	Genotyping

Table S1. Related to Key Resources Table subheading “Oligonucleotides”.

Shown are all oligonucleotides used in this study and their purpose in QPCR, or Genotyping.

Figure 1

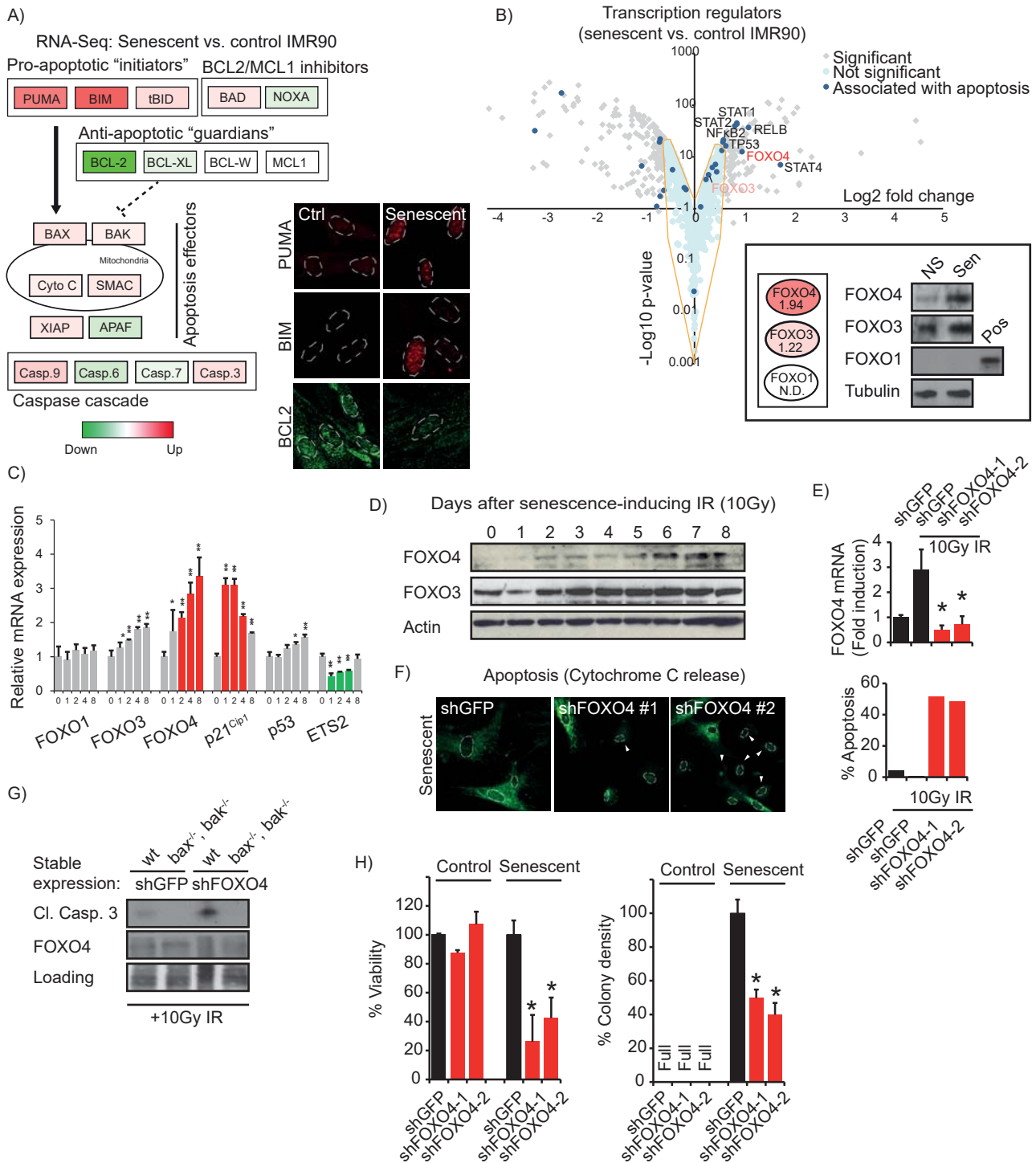


Figure 2

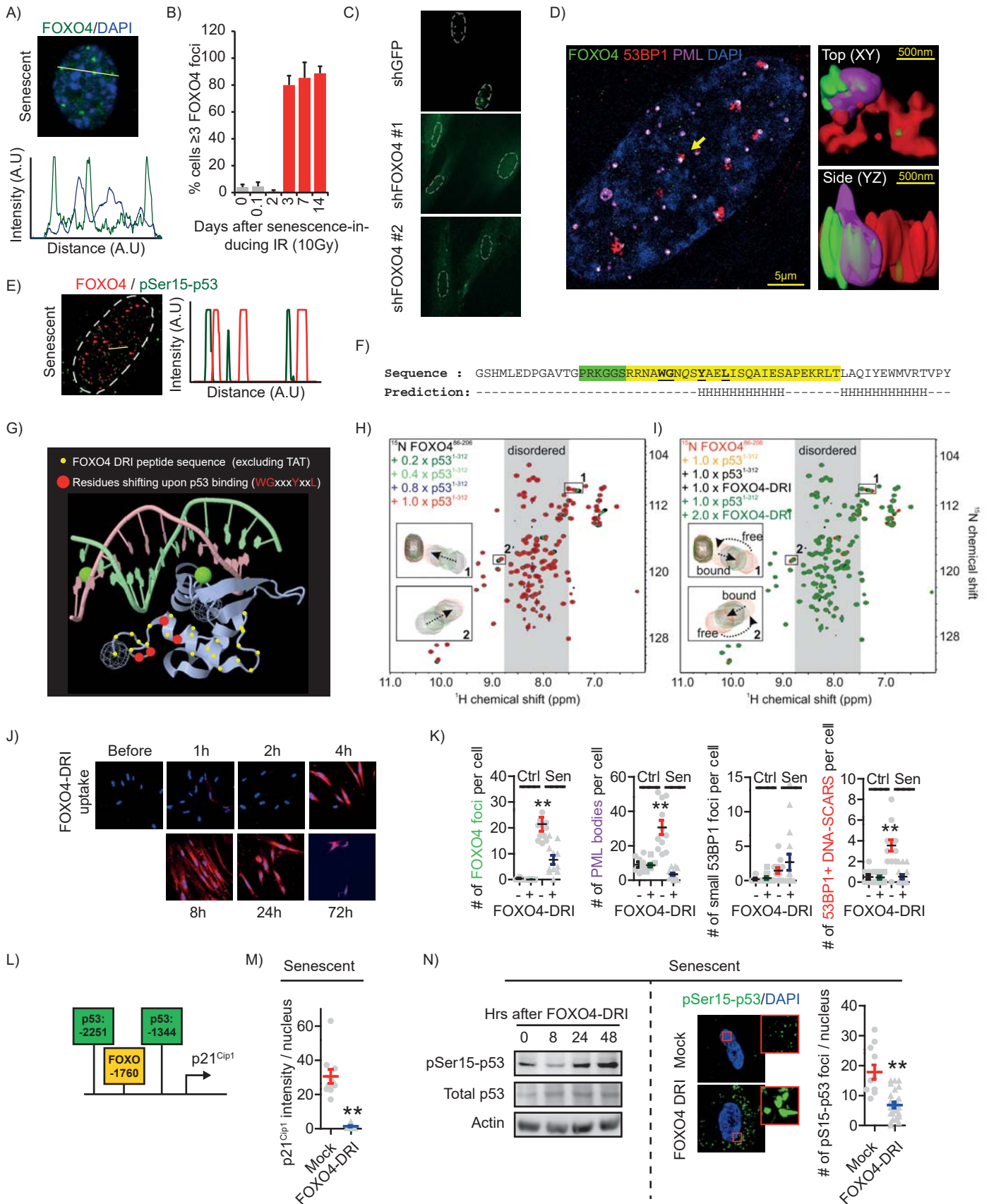


Figure 3

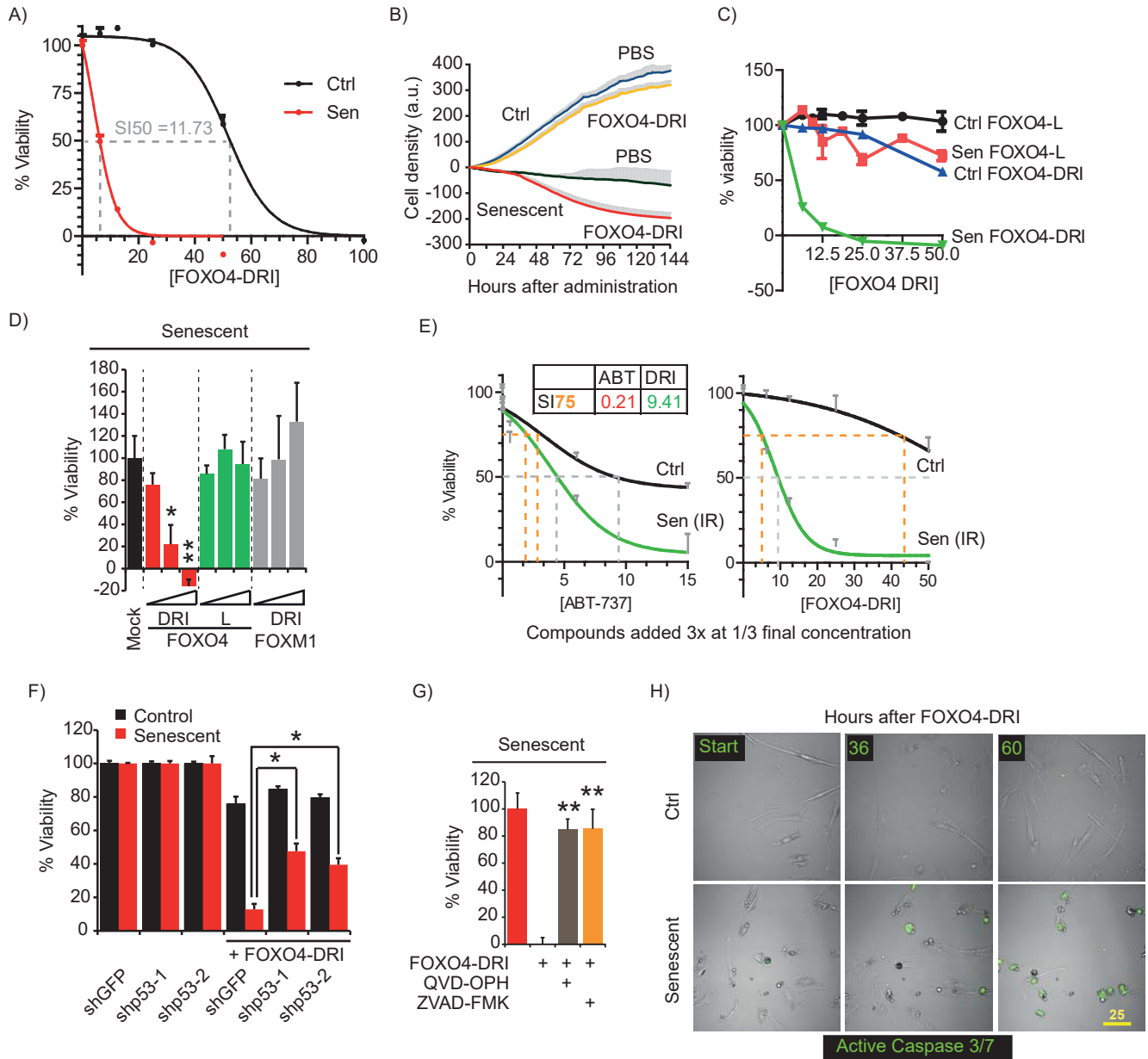


Figure 4

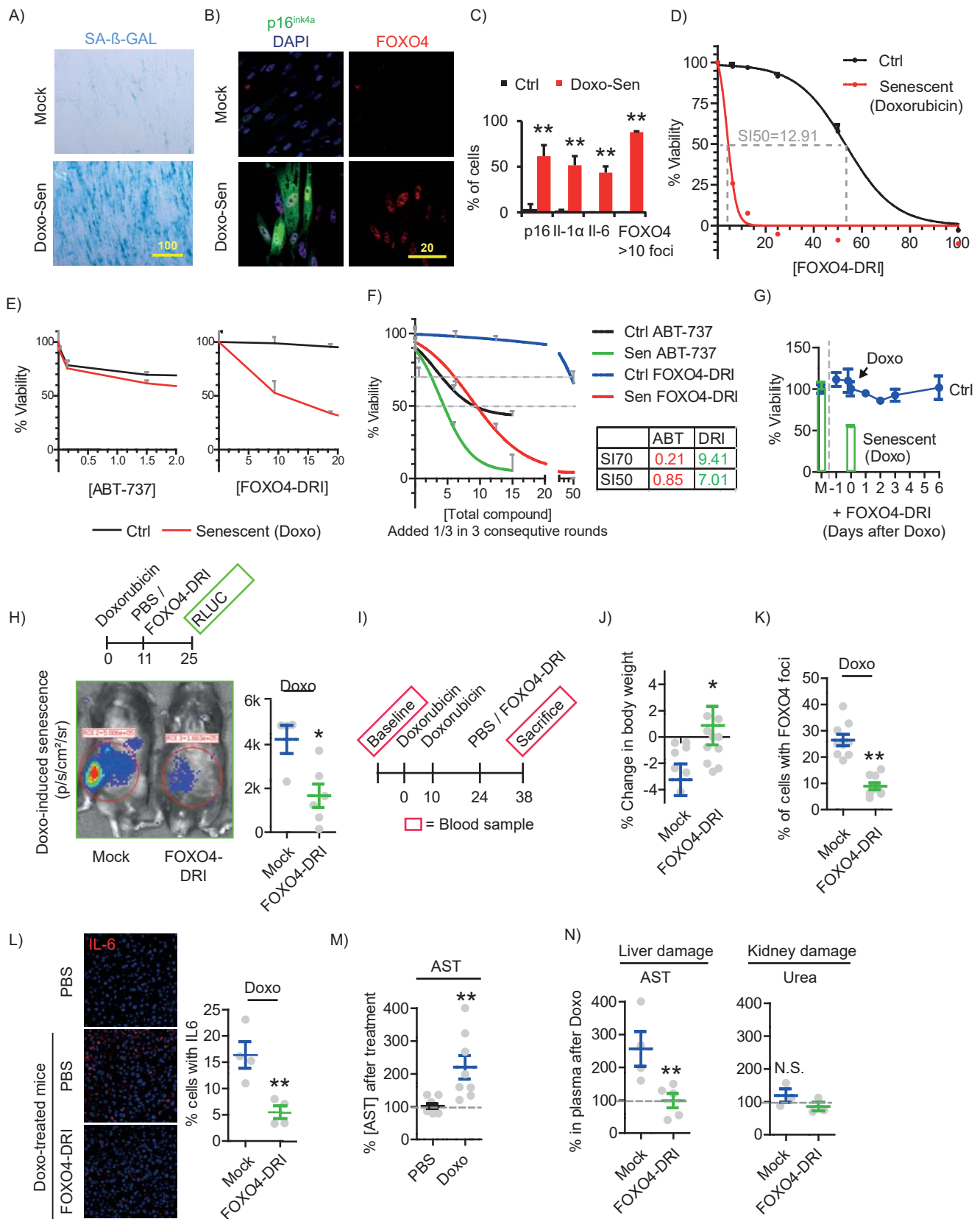


Figure 5

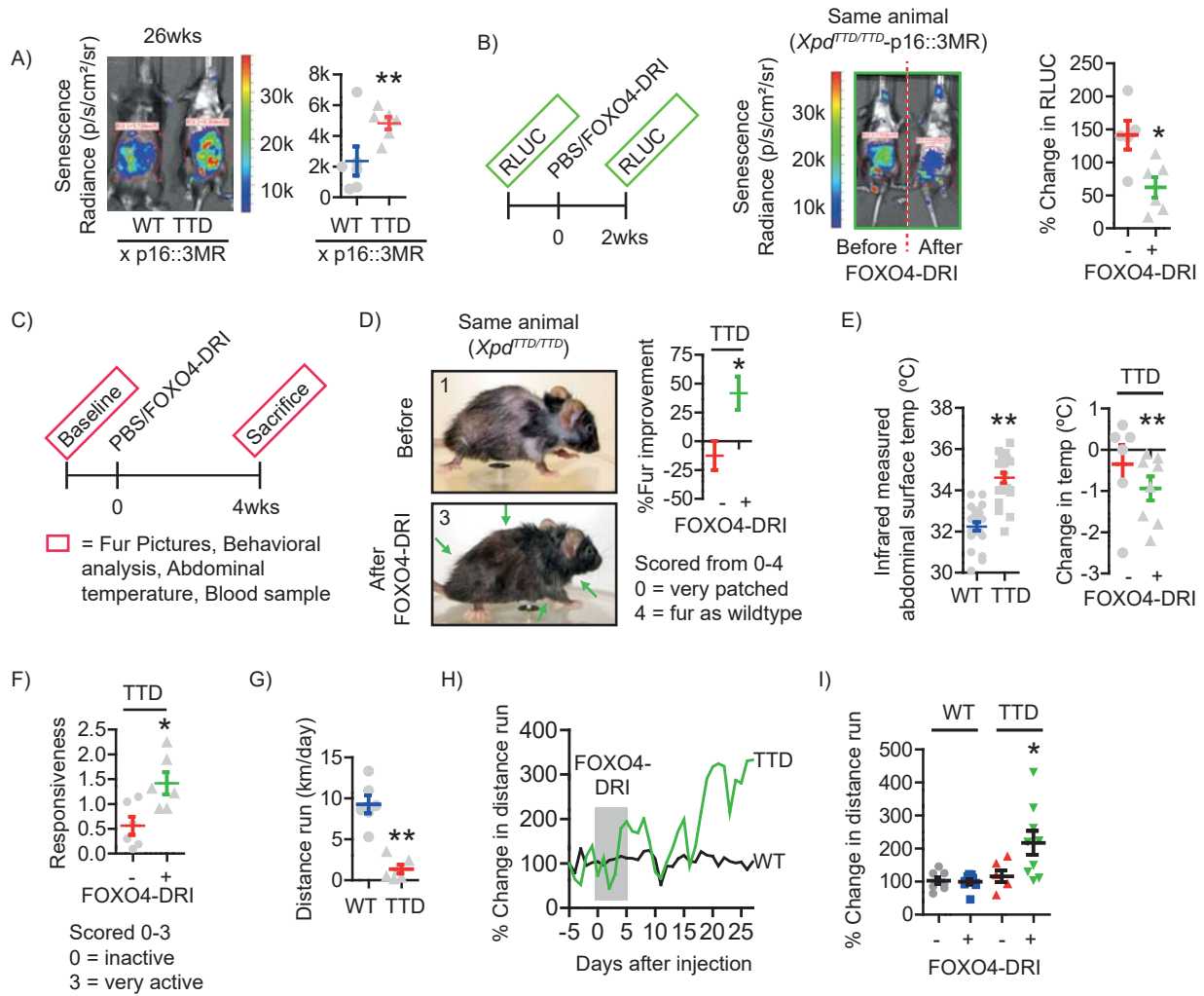


Figure 6

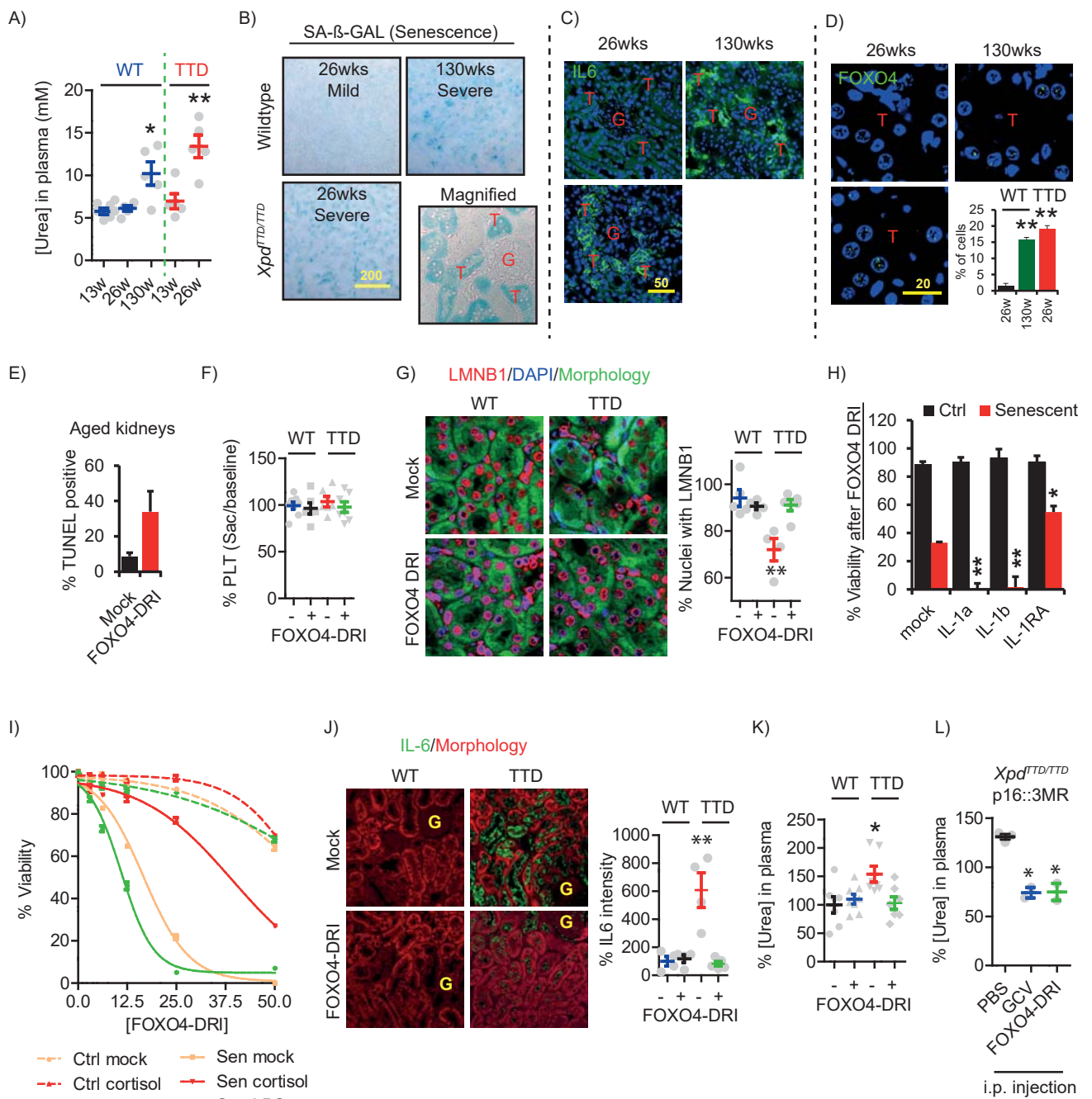
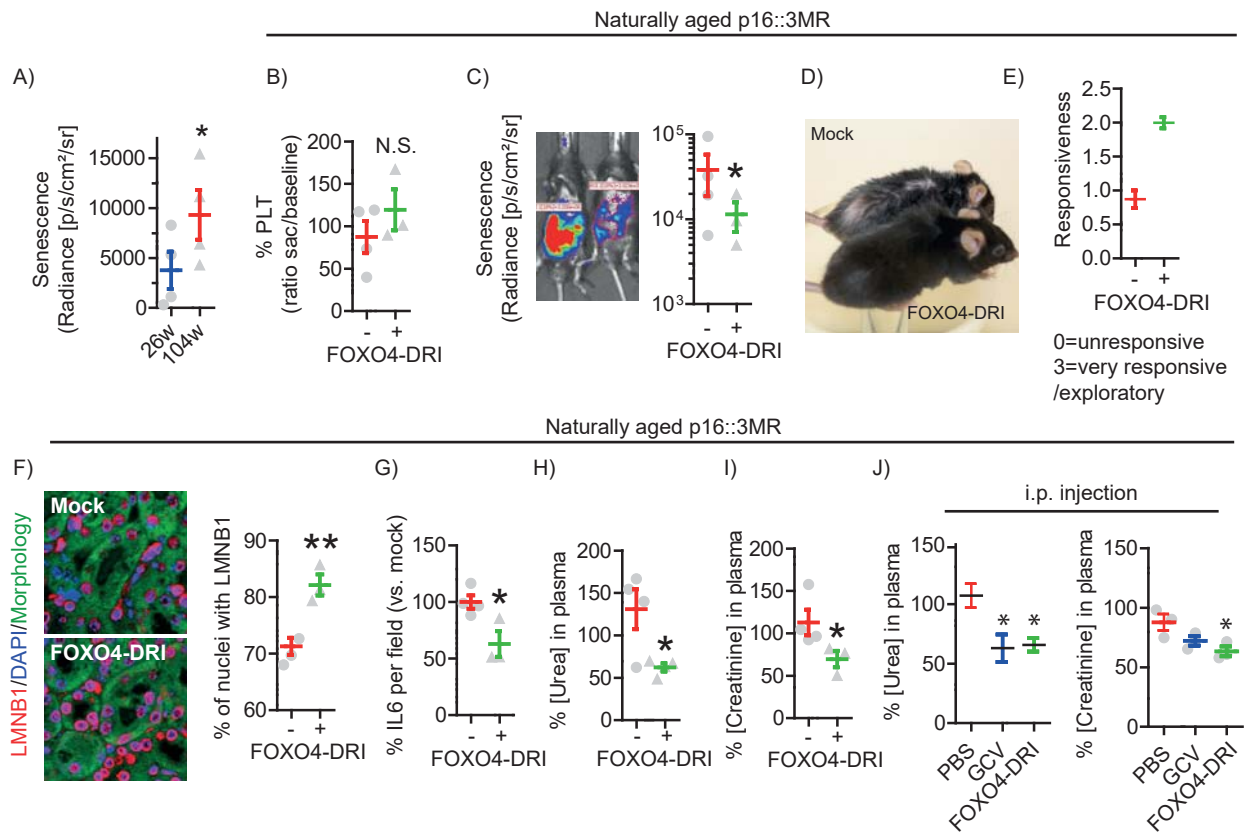


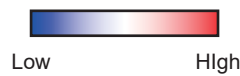
Figure 7



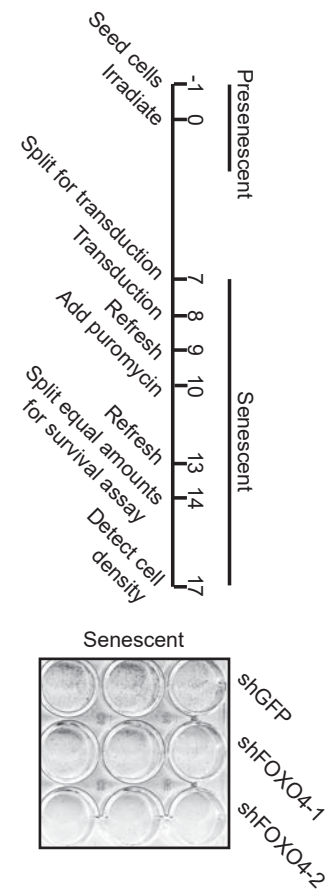
Supplementary figure 1

A)

Name	Ctrl	Sen	F.C.	p-value
TP53INP1			2.83	1.06E-80
TP53			1.55	4.78E-17
PUMA			2.59	5.06E-26
BIM			3.56	4.55E-12
tBID			1.31	5.19E-08
BAD			1.17	8.71E-04
NOXA			-1.20	6.98E-03
Survivin			-12.95	0.00E+00
BCL2			-5.00	4.25E-19
BCL-XL			-1.13	8.80E-03
MCL1			1.03	4.35E-01
BCL-W			1.20	8.64E-05
BAK			1.01	8.83E-01
BAX			1.17	1.91E-03
Cytochrome C			1.04	3.53E-01
SMAC			1.11	2.53E-02
XIAP			1.16	7.07E-03
APAF1			-1.46	6.57E-10
Caspase-9			1.48	2.45E-05
Caspase-3			1.22	7.22E-05
Caspase-6			-1.42	6.23E-06
Caspase-7			-1.03	9.33E-01
FADD			-1.22	1.30E-04
TRADD			1.16	1.77E-02
Caspase-8			1.42	2.37E-05

Difference in mRNA expression
vs. average between groups

C)



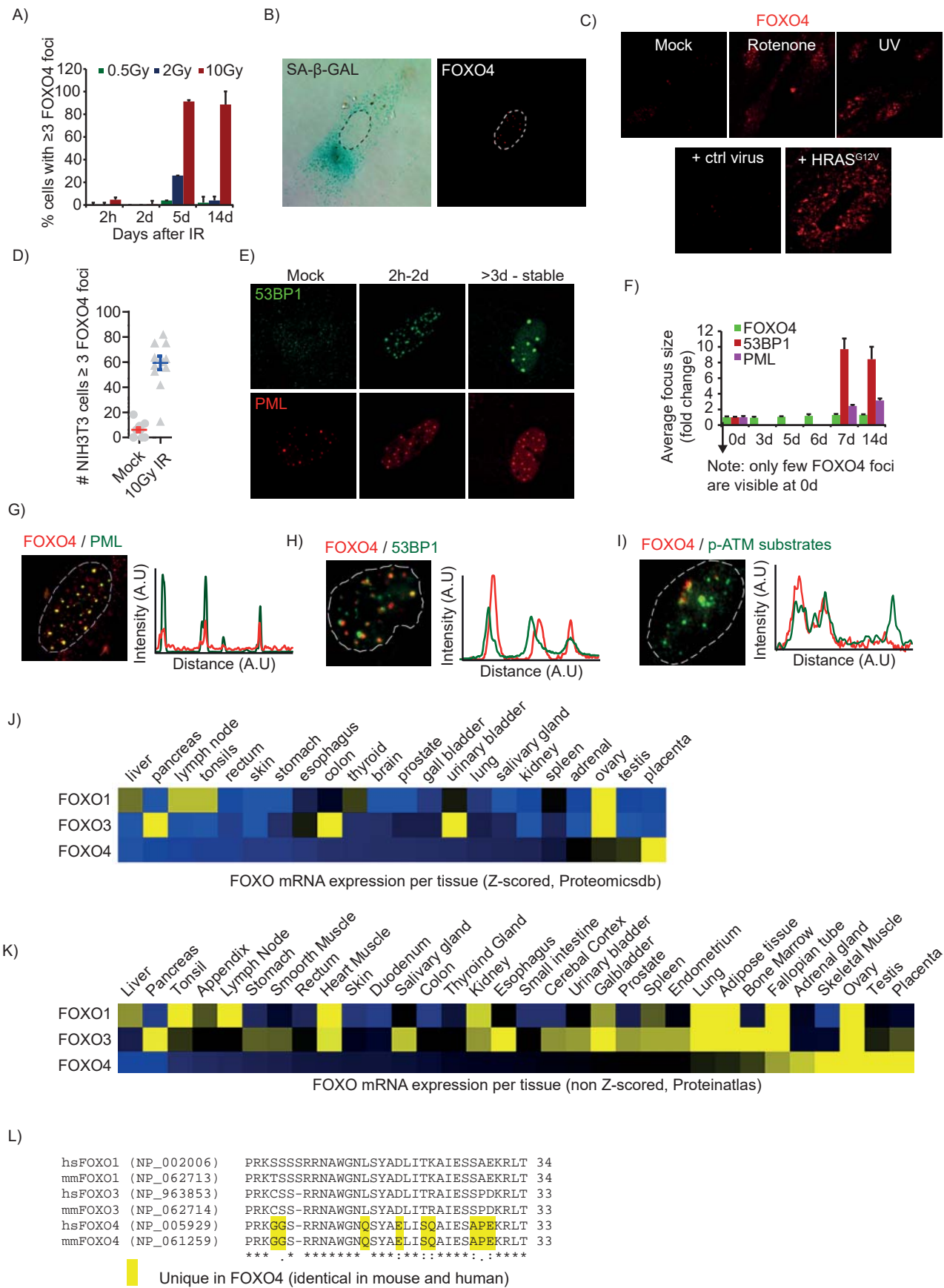
B)

Name	Full name	Fold change	p-value
E2F2	E2F transcription factor 2	0.11	9.32E-33
E2F1	E2F transcription factor 1	0.16	9.83E-173
FOS	FBJ murine osteosarcoma viral oncogene homolog	0.48	2.07E-07
IRF6	interferon regulatory factor 6	0.59	7.93E-02
E2F3	E2F transcription factor 3	0.61	4.69E-20
FOSB	FBJ murine osteosarcoma viral oncogene homolog B	0.62	1.84E-02
STAT5B	signal transducer and activator of transcription 5B	0.62	6.86E-23
MSX1	msh homeobox 1	0.65	5.60E-03
STAT5A	signal transducer and activator of transcription 5A	0.74	2.33E-06
E2F4	E2F transcription factor 4, p107/p130-binding	0.87	2.95E-03
RELA	v-rel reticuloendotheliosis viral oncogene homolog A (avian)	0.89	4.65E-03
JUNB	jun B proto-oncogene	0.99	9.44E-01
MYC	v-myc myelocytomatosis viral oncogene homolog (avian)	1.09	8.34E-02
NFKB1	nuclear factor of kappa light polypeptide gene enhancer in B-cells 1	1.17	2.22E-04
FOXO3	forkhead box O3	1.22	3.01E-05
MAX	MYC associated factor X	1.28	5.99E-07
IRF9	interferon regulatory factor 9	1.34	7.00E-08
TRPS1	trichorhinophalangeal syndrome I	1.36	7.50E-06
JUND	jun D proto-oncogene	1.47	4.65E-14
STAT3	signal transducer and activator of transcription 3 (acute-phase response factor)	1.49	5.23E-20
STAT6	signal transducer and activator of transcription 6, interleukin-4 induced	1.50	6.90E-22
TP53	tumor protein p53	1.55	4.78E-17
STAT1	signal transducer and activator of transcription 1, 91kDa	1.76	1.51E-40
STAT2	signal transducer and activator of transcription 2, 113kDa	1.80	9.54E-46
NFKB2	nuclear factor of kappa light polypeptide gene enhancer in B-cells 2 (p49/p100)	1.81	9.62E-44
FOXO4	forkhead box O4	1.94	2.52E-13
RELB	v-rel reticuloendotheliosis viral oncogene homolog B	2.12	1.07E-37
STAT4	signal transducer and activator of transcription 4	3.32	9.35E-08

Significantly down

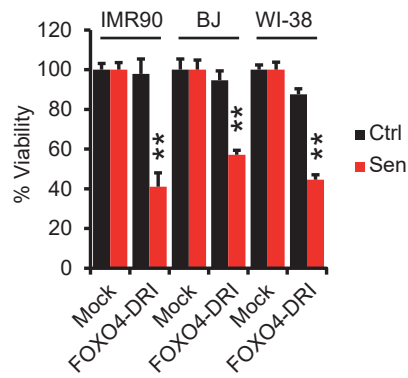
Significantly up

Supplementary figure 2

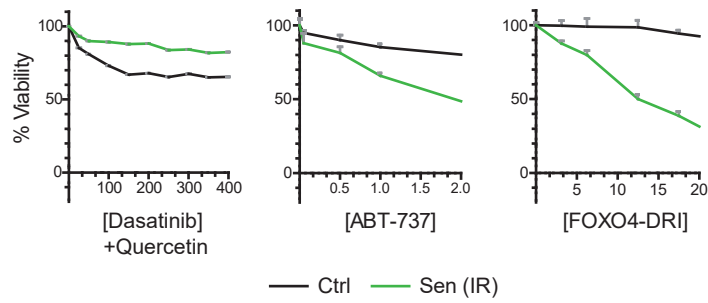


Supplementary figure 3

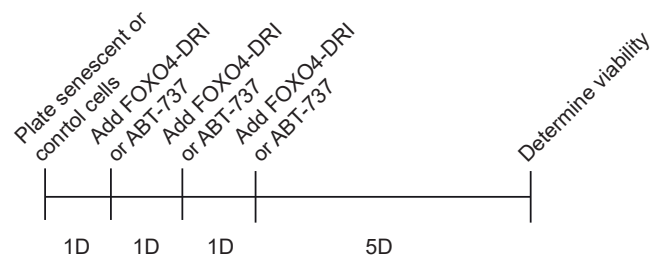
A)



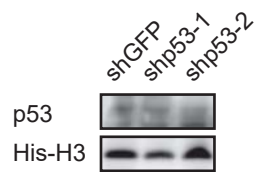
B)



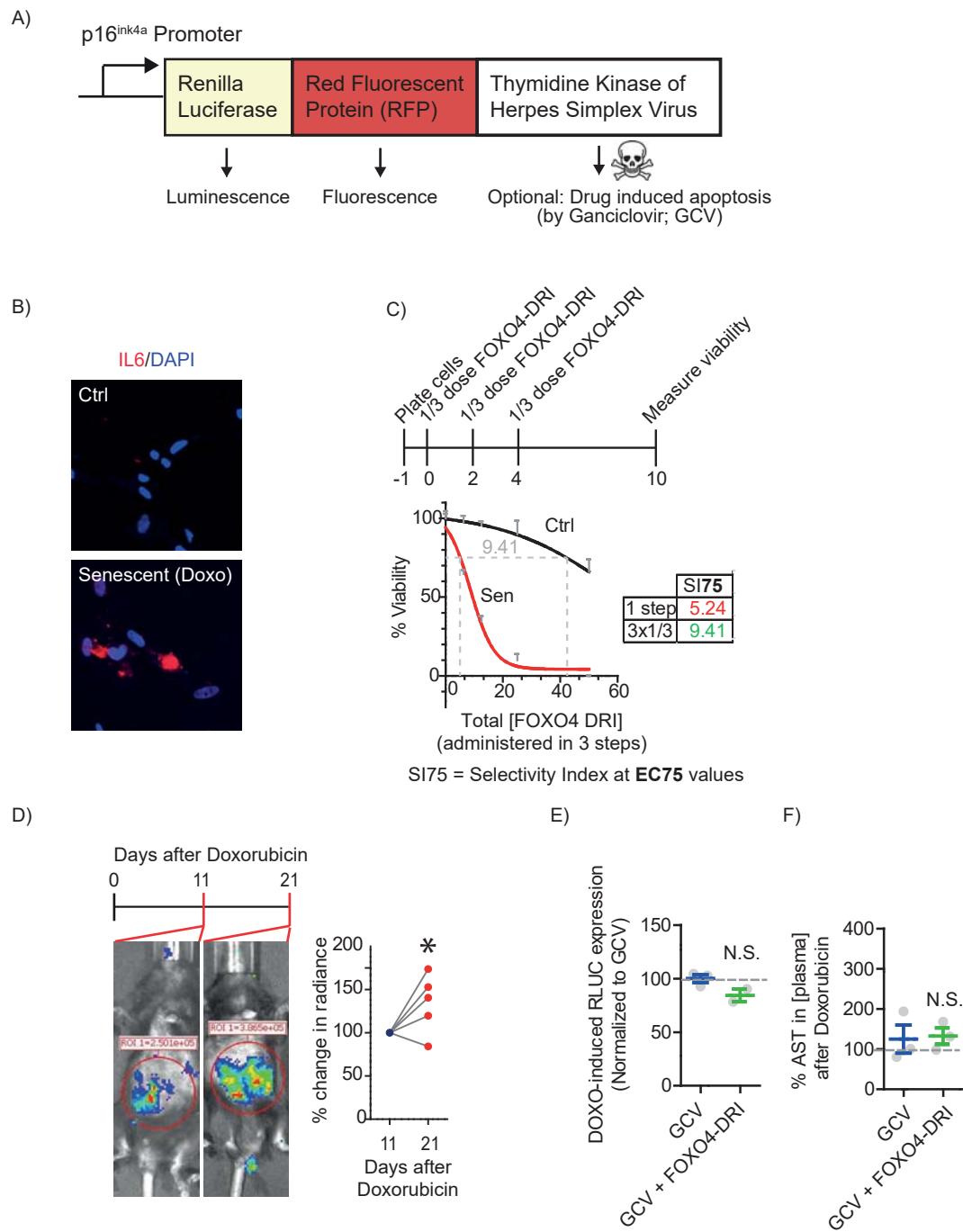
C)



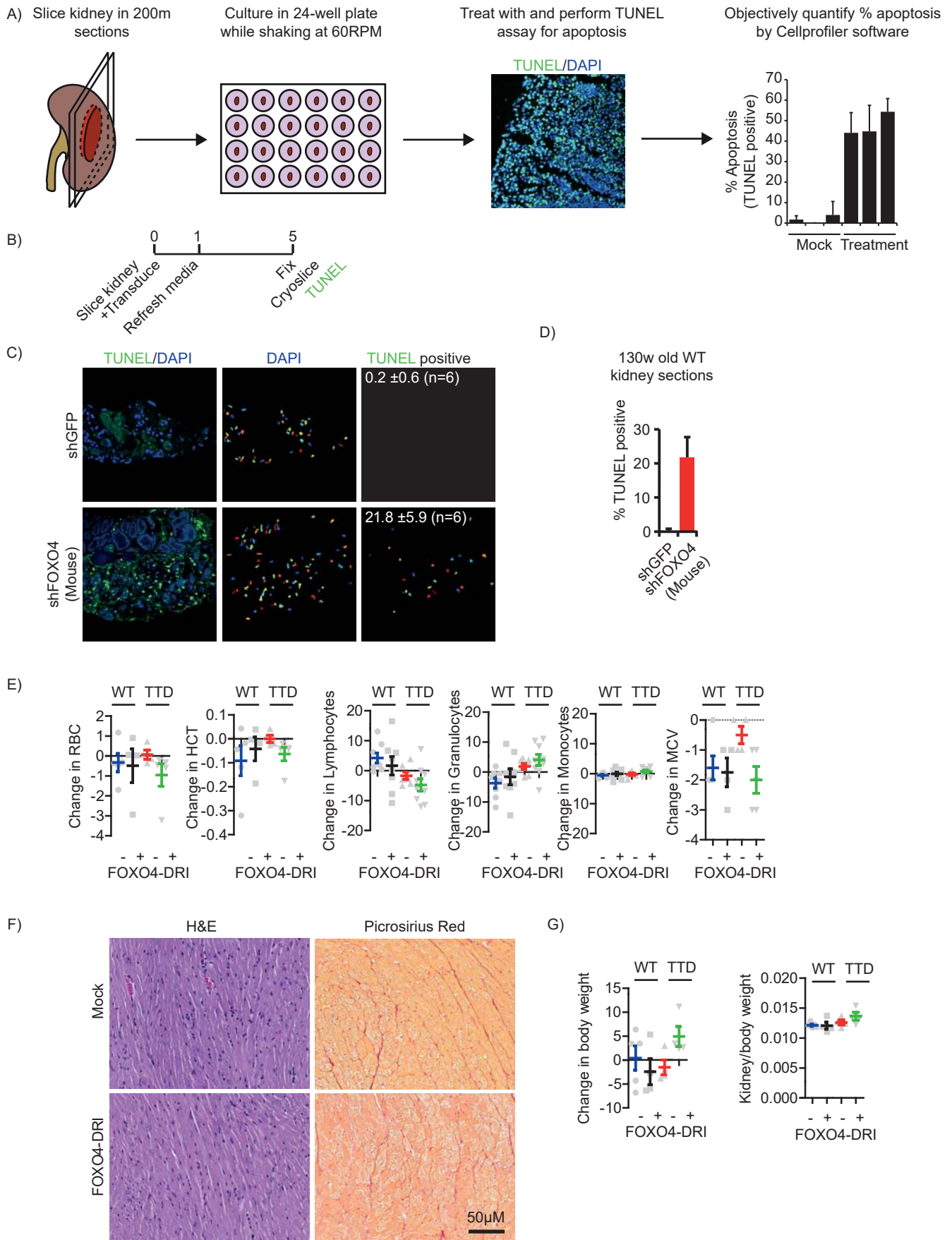
D)



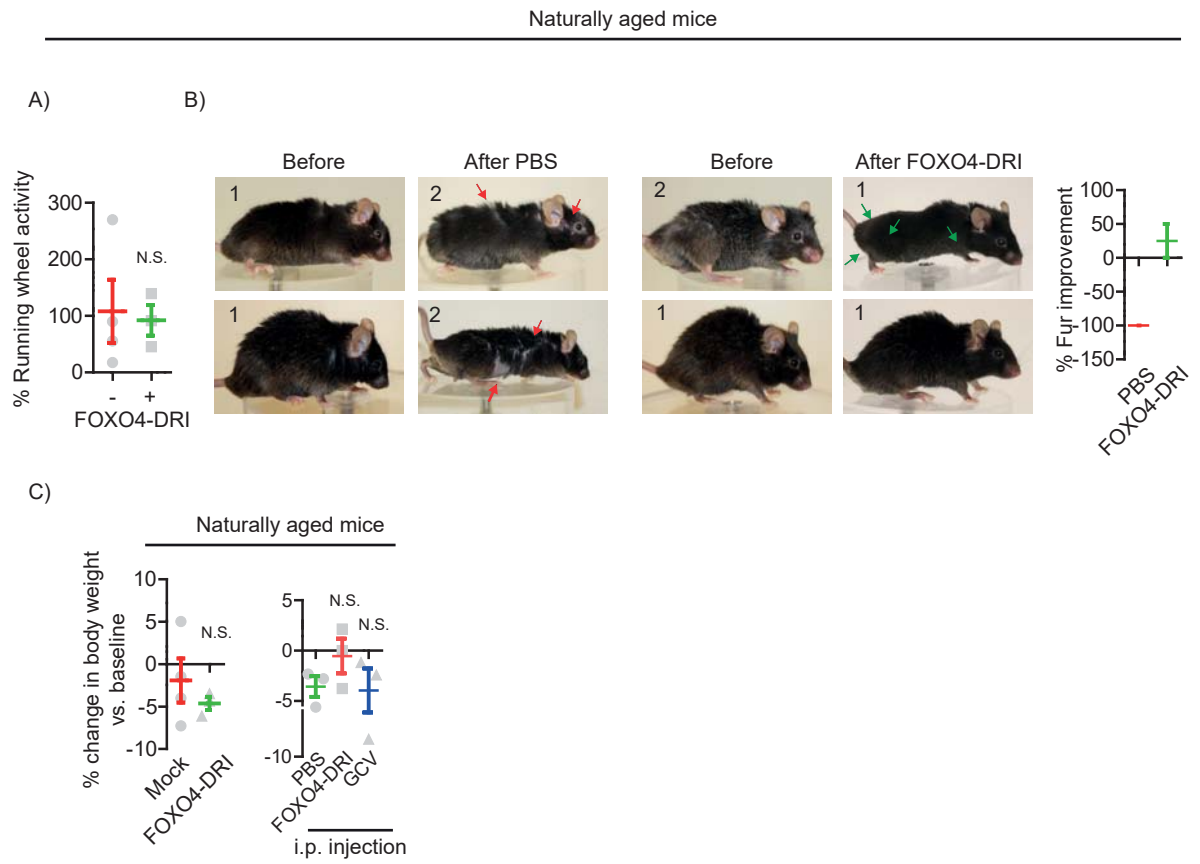
Supplemental Figure 4



Supplementary figure 6



Supplementary figure 7

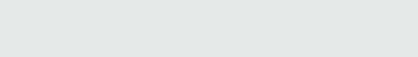




Click here to access/download

Supplemental Movies and Spreadsheets

Mov1 - SIM Senescent Nucleus FOXO4-G 53BP1-R
RPML-P.avi





[Click here to access/download](#)

Supplemental Movies and Spreadsheets

Mov2 - 3D SIM Senescent Nucleus FOXO4-G 53BP1-R
PML-P.avi



[Click here to access/download](#)

Supplemental Movies and Spreadsheets

Mov3 - Ctrl cells +FOXO4 DRI - Caspase3-7Green.wmv





Click here to access/download

Supplemental Movies and Spreadsheets

Mov4 - Senescent cells +FOXO4 DRI - Caspase3-
7Green.wmv